Philosophical Magazine
Vol. 00, No. 00, 00 Month 200x, 1–24

RESEARCH ARTICLE

On the macroscopic response, microstructure evolution, and macroscopic stability of short-fiber-reinforced elastomers at finite strains: II—Representative examples

Reza Avazmohammadi, Pedro Ponte Castañeda

Department of Mechanical Engineering and Applied Mechanics, University of Pennsylvania, Philadelphia, PA 19104-6315, U.S.A.

(*Received 00 Month 200x; final version received 00 Month 200x*)

In Part I of this work, we presented a homogenization-based constitutive model for the overall behavior of reinforced elastomers consisting of aligned, spheroidal particles distributed randomly in an incompressible, hyperelastic matrix. In particular, we provided analytical estimates for the effective stored-energy functions of the composites, as well as for the associated average particle rotations under finite deformations. The rotation of the particles is found to be very sensitive to the specific loading conditions applied, and is such that the particles tend to align themselves with the largest tensile direction. In addition, we obtained corresponding formulae for the detection of macroscopic instabilities in these composites. With the objective of illustrating the key features of the analytical results presented in Part I, we conduct here a more detailed study of these results for several representative values of the microstructural and loading parameters, as well as matrix properties. More specifically, this study deals with neo-Hookean and Gent elastomers reinforced with spheroidal particles of prolate and oblate shapes with various aspect ratios and volume fractions, subjected to aligned and non-aligned macroscopic loading conditions. In addition, to assess the accuracy of the model, we compare our results with corresponding finite element results available from the literature for the special case of spherical particles, and good agreement is found. For non-spherical particles, the results indicate that the possible rotation of the particles has a major influence on the overall response of the elastomeric composites. Furthermore, it is found that the composite may develop macroscopic shear localization instabilities, as a consequence of the geometric softening induced by the sudden rotation—or flopping—of the particles, when a sufficiently large amount of compression is applied along the long axes of the particles.

Keywords: microstructure; large deformation; bifurcation; flopping-type instability; geometric softening

1. Introduction

In the preceding paper, henceforth referred to as Part I, we made use of a recently developed, improved version [3] of the tangent second-order (TSO) homogenization method to determine estimates for the macroscopic elastic behavior of short-fiber-reinforced elastomers. More specifically, the class of composites considered in this work consists of (incompressible) generalized neo-Hookean elastomers reinforced by aligned, rigid, spheroidal particles of identical aspect ratios (see Fig. 1 in Part I), exhibiting overall transversely isotropic behavior in the undeformed configuration. The composite is subjected to finite-deformation loadings whose principal stretching directions are generally not aligned with those of the particles in the undeformed configuration. The analytical estimates, presented in Part I, include estimates for the effective stored-energy function of the composite, denoted by $\widehat{W}$, as well as the associated finite rotations of the particles, denoted by $\bar{\boldsymbol{\psi}}^{(2)}$, which are a consequence of the large deformations involved. Moreover, we investigate the possible development of macroscopic instabilities in the composite, which, as discussed in Part I, correspond to loss of strong ellipticity of the effective stored-energy function $\widehat{W}$.

Our aim in Part II of this work is to examine, in the context of some representative examples, the essential features of the effective constitutive model for the composites

ISSN: 1478-6435 print/ISSN 1478-6443 online

DOI: 10.1080/14786435.20xx.xxxxxx
http://www.informaworld.com

provided in Part I. In particular, we investigate the influence of the relevant microstructural variables (particle aspect ratio and volume fraction), as well as nonlinear behavior of the matrix phase, on the effective stored-energy function, appropriate macroscopic stress measures and possible change in orientation of the underlying particles. In this connection, it should be noted that the results given here for *dilute* concentrations of particles can be viewed as a generalization of the Eshelby results in linear elasticity to finite elasticity. Moreover, we investigate the influence of the microstructural variables on the possible development of macroscopic instabilities in the composites, as determined by the strong ellipticity condition. Along these lines, we will also explore the connections between the rotation of the particles and the macroscopic instabilities. Specifically, we provide results for the two special classes of macroscopic loadings discussed in Part I, namely, *axisymmetric shear* and *pure shear* loading conditions. Both of these types of loadings will be considered for *aligned* and *non-aligned* conditions.

The outline of the paper is as follows. In section 2, for convenience and clarity, we briefly recall the analytical results presented in Part I and lay out the key features of the results to be studied in this paper. Making use of these results, in section 3 we provide and discuss examples for various microgeometries, matrix properties and loading parameters. In particular, in this section, we put into evidence the interplay between the rotation of the particles under non-aligned large deformations and the geometric softening observed in the associated macroscopic behavior. We also show that the macroscopic instabilities that develop in the particle-reinforced composites are basically caused by the collective rotation—or "*flopping*"—of the particles, when compressed along their long axes. Finally, in Section 4, we provide some concluding remarks.

2. Overall constitutive behavior

In this section, we briefly recall the analytical results presented in Part I and the associated sets of examples to be provided in this paper. In Part I, we considered two-phase composites consisting of an incompressible, elastomeric matrix phase (phase 1), characterized by the stored-energy function $W_\mu^{(1)}$, and a polydisperse family of rigid, aligned, spheroidal particles (phase 2) with aspect ratio w and volume fraction c. For definiteness, the principal directions of the particles in the undeformed configuration are defined by the rectangular Cartesian basis $\{\mathbf{e}_i\}$ such that the symmetry axis of the particles is aligned with the $\mathbf{e}_3$ direction in that configuration. Also, the distribution of particles is assumed to be statistically isotropic in the transverse plane, which is the plane perpendicular to the symmetry axis of particles, namely, the $\mathbf{e}_1-\mathbf{e}_2$ plane. For convenience, the basis $\{\mathbf{e}_i\}$ is taken to define the fixed laboratory frame of reference as well, and henceforth, unless stated, the components of any tensorial quantity will be referred to $\{\mathbf{e}_i\}$. Moreover, two different geometries for the particles are assumed: (i) *prolate* $(w \geq 1)$ and (ii) *oblate* $(w < 1)$ spheroidal particles (see Figs. 1(a), (b) in Part I.) Furthermore, in Part I, the *local* constitutive behavior of the matrix phase was assumed to be characterized by a fairly general class of incompressible, isotropic stored-energy functions, written as

$$W_\mu^{(1)}(\mathbf{F}) = g(I) + h(J), \tag{1}$$

where g and h are material functions, and $I = \mathrm{tr}(\mathbf{F}^T\mathbf{F}) = \lambda_1^2+\lambda_2^2+\lambda_3^2$ and $J = \det\mathbf{F} = \lambda_1\lambda_2\lambda_3$ denote, respectively, the first and third invariants of the deformation gradient tensor $\mathbf{F}$, with $\lambda_1, \lambda_2, \lambda_3$ identifying the corresponding principal stretches. Here, the deformation gradient $\mathbf{F}$ is subject to the incompressibility constraint, implying that

$$\det\mathbf{F} = \lambda_1\lambda_2\lambda_3 = 1. \tag{2}$$

In this paper, for calculation purposes, we make use of two simple examples of (1). The first material is a neo-Hookean solid whose stored-energy function is given by

$$W_\mu^{(1)}(\mathbf{F}) = \frac{1}{2}\mu^{(1)}(I-3) + \frac{1}{2}\mu^{(1)}(J-1)\,(J-3). \tag{3}$$

where $\mu^{(1)}$ is the shear modulus of the solid at zero strain. The second material is an incompressible Gent solid with stored-energy function

$$W_\mu^{(1)}(\mathbf{F}) = -\frac{J_m\,\mu^{(1)}}{2}\ln\left(1-\frac{I-3}{J_m}\right) + \frac{1}{2}\mu^{(1)}(J-1)\,(J-3) - \frac{\mu^{(1)}}{J_m}(J-1)^2, \tag{4}$$

where $J_m(>0)$ is the *lock-up* parameter serving to characterize the the limiting chain extensibility of elastomers. It is noted that the neo-Hookean model (3) corresponds to the limit as J_m approaches infinity of the the Gent model (4), and does not lock up at finite strain. It is also recalled that the terms involving the factor $(J-1)$ do not vanish for the homogenized behavior of the reinforced elastomers and are in fact crucial to obtain the correct linearized behavior (see part I).

The above-described particle-reinforced material is a *transversely isotropic* composite (with symmetry axis aligned with $\mathbf{e}_3$) in the undeformed configuration, and its macroscopic response is characterized by the effective stored-energy function $\widehat{W}(\bar{\mathbf{F}})$. The macroscopic deformation gradient $\bar{\mathbf{F}}$ is subject to the *exact* overall incompressibility constraint $\det(\bar{\mathbf{F}}) = \bar{\lambda}_1\bar{\lambda}_2\bar{\lambda}_3 = 1$, with $\bar{\lambda}_1, \bar{\lambda}_2, \bar{\lambda}_3$ identifying the macroscopic principal stretches. For definiteness in the analytical calculations, and motivated by possible comparisons with numerical simulations and/or experiments, we consider deformation gradients $\bar{\mathbf{F}}$ with the matrix representation

$$[\bar{F}_{ij}] = \begin{bmatrix} \cos(\bar{\theta}) & 0 & \sin(\bar{\theta}) \\ 0 & 1 & 0 \\ -\sin(\bar{\theta}) & 0 & \cos(\bar{\theta}) \end{bmatrix} \begin{bmatrix} \bar{\lambda}_1 & 0 & 0 \\ 0 & \bar{\lambda}_2 & 0 \\ 0 & 0 & (\bar{\lambda}_1\bar{\lambda}_2)^{-1} \end{bmatrix} \begin{bmatrix} \cos(\bar{\theta}) & 0 & -\sin(\bar{\theta}) \\ 0 & 1 & 0 \\ \sin(\bar{\theta}) & 0 & \cos(\bar{\theta}) \end{bmatrix}, \tag{5}$$

where the conditions $\bar{\lambda}_1 = \bar{\lambda}_2 = \bar{\lambda}$ and $\bar{\lambda}_1 = \bar{\lambda}$, $\bar{\lambda}_2 = 1$ correspond respectively to axisymmetric and pure shear loadings, with $\bar{\lambda}$ denoting a positive loading parameter. In the above representation, $\bar{\theta}$ denotes the angle of the Lagrangian principal loading axes relative to the (fixed) basis $\{\mathbf{e}_i\}$ in the $\mathbf{e}_1-\mathbf{e}_3$ plane. Also, for convenience, we let the directions of the principal stretches $\bar{\lambda}_1, \bar{\lambda}_2, \bar{\lambda}_3 = (\bar{\lambda}_1\bar{\lambda}_2)^{-1}$ be identified with the Cartesian vectors $\{\mathbf{e}_i'\}$ $(i=1,2,3)$. A schematic representation of the particle-reinforced elastomers subjected to the class of loadings (5) is given in Fig. 3 of Part I.

In Part I, we made use of the tangent second-order (TSO) procedure of Avazmohammadi and Ponte Castañeda [3] to generate estimates for the effective stored-energy function $\widehat{W}(\bar{\mathbf{F}})$ of the above-described particle-reinforced materials, which, under deformation gradient (5), takes the functional form

$$\widehat{W}(\bar{\mathbf{F}}) = \widehat{\phi}(\bar{\lambda}_1, \bar{\lambda}_2, \bar{\theta}), \tag{6}$$

and is given explicitly by equation (31) in Part I. Also, as discussed in Part I, the principal directions of loading (identified by the $\{\mathbf{e}_i'\}$ axes) are, in general, not aligned with those of the particles (identified by the $\{\mathbf{e}_i\}$ axes in the undeformed configuration), leading to finite changes in the orientation of particles as characterized by the angle $\bar{\psi}^{(2)}$. An estimate for this angle, which is an essential part in the estimate for $\widehat{\phi}$, is delivered by the TSO procedure and given by equation (33) in Part I. In addition, Eqs. (59)-(62) and (65)-(68) in Part I provide the associated *strong ellipticity* (SE) conditions

for the composites under aligned loadings, for axisymmetric and pure shear loading conditions, respectively. Likewise, Eqs. (57) and (63) provide the SE conditions for the composites under non-aligned loadings for axisymmetric and pure shear loading conditions, respectively. Before proceeding with the detailed examples, it proves helpful to provide a brief description of the three different types of results covered in this paper.

Effective constitutive relation.

Recalling that the fiber-reinforced elastomers of interest in this work are incompressible, their macroscopic constitutive relation is determined by the following expression for the average Cauchy stress tensor

$$\bar{\mathbf{T}} = \frac{\partial \widehat{W}(\bar{\mathbf{F}})}{\partial \bar{\mathbf{F}}} (\bar{\mathbf{F}})^T - p\mathbf{I}, \tag{7}$$

where p stands for the arbitrary hydrostatic pressure associated with the incompressibility constraint.

For the specific purpose of discussing the axisymmetric and pure shear modes of loading, it is useful to introduce the scalar stress variables

$$\bar{S}^{AS} = \frac{\partial \widehat{\phi}^{AS}(\bar{\lambda},\bar{\theta})}{\partial \bar{\lambda}}, \text{ and } \bar{S}^{PS} = \frac{\partial \widehat{\phi}^{PS}(\bar{\lambda},\bar{\theta})}{\partial \bar{\lambda}}, \tag{8}$$

where (recalling expression (6)) $\widehat{\phi}^{AS} = \widehat{\phi}(\bar{\lambda},\bar{\lambda},\bar{\theta})$ and $\widehat{\phi}^{PS} = \widehat{\phi}(\bar{\lambda},1,\bar{\theta})$, respectively. They can be related to the normal components of the macroscopic *Cauchy stress* tensor $\bar{\mathbf{T}}$ via the relations

$$\bar{S}^{AS} = \bar{\lambda}^{-1}\left[\left(\bar{T}'_{11}+\bar{T}'_{22}\right) - 2\bar{T}'_{33}\right], \text{ and } \bar{S}^{PS} = \bar{\lambda}^{-1}\left(\bar{T}'_{11}-\bar{T}'_{33}\right), \tag{9}$$

where the $\bar{T}'_{ij}$ denote the components of the tensor $\bar{\mathbf{T}}$ relative to the "loading" basis $\{\mathbf{e}'_i\}$ (see Fig. 3 in Part I), and are determined by transformation rule

$$\bar{T}'_{ij} = \bar{Q}_{pi}\bar{T}_{pq}\bar{Q}_{qj}, \tag{10}$$

with $\bar{\mathbf{Q}} = \cos(\bar{\theta})(\mathbf{e}_1\otimes\mathbf{e}_1+\mathbf{e}_3\otimes\mathbf{e}_3) + \sin(\bar{\theta})(\mathbf{e}_1\otimes\mathbf{e}_3-\mathbf{e}_3\otimes\mathbf{e}_1) + \mathbf{e}_2\otimes\mathbf{e}_2$. Note that for the case of aligned loadings ($\bar{\theta}=0^\circ$), the effective stored-energy functions $\widehat{\phi}^{AS}$ and $\widehat{\phi}^{PS}$ are explicitly given by Eqs. (39) and (42) in Part I, and the associated stress measures read as $\bar{S}^{AS} = \bar{\lambda}^{-1}\left[(\bar{T}_{11}+\bar{T}_{22}) - 2\bar{T}_{33}\right]$ and $\bar{S}^{PS} = \bar{\lambda}^{-1}(\bar{T}_{11}-\bar{T}_{33})$, where it is recalled that the particles are initially aligned in the $\mathbf{e}_3$ direction.

Moreover, for dilute concentrations of particles, it proves useful to consider the following *modified* effective stress measures

$$\bar{S}_0^{AS} = \frac{\partial \widehat{\phi}_0^{AS}(\bar{\lambda},\bar{\theta})}{\partial \bar{\lambda}}, \quad \bar{S}_0^{PS} = \frac{\partial \widehat{\phi}_0^{PS}(\bar{\lambda},\bar{\theta})}{\partial \bar{\lambda}}, \tag{11}$$

where $\widehat{\phi}_0^{PS}(\bar{\lambda},\bar{\theta})$ and $\widehat{\phi}_0^{AS}(\bar{\lambda},\bar{\theta})$ are given by

$$\widehat{\phi}_0^{AS} = \frac{1}{c}\left(\widehat{\phi}^{AS} - \phi^{AS}\right), \quad \widehat{\phi}_0^{PS} = \frac{1}{c}\left(\widehat{\phi}^{PS} - \phi^{PS}\right), \tag{12}$$

with ϕ^{AS} and ϕ^{PS} denoting the stored-energy function of the homogeneous matrix phase evaluated at the appropriate deformation gradients.

Evolution of microstructure. As discussed in Part I, the TSO procedure for estimating the effective stored-energy function $\widehat{W}(\bar{\mathbf{F}})$ also accounts for the evolution of the underlying microstructure, resulting from the finite changes in geometry that are induced by the deformation. Information on the variables characterizing the evolution of the microstructure provides deeper physical insight into the observed macroscopic behavior. For the class of particle-reinforced composites under study, the volume fraction and shape of the particles do not change (because the particles are rigid and the matrix is incompressible), and the only microstructural variables that evolve with the deformation are the orientation of the particles, and the shape and orientation of the distributional ellipsoid characterizing the angular dependence of the two-point correlation function (for the distribution of the particle centers). As we have seen, the TSO model provides us with direct access to the rotation of the particles ($\bar{\psi}^{(2)}$, as given by Eq. (33) in Part I). For aligned loadings ($\bar{\theta} = 0^\circ$), the particle do not rotate ($\bar{\psi}^{(2)} = 0^\circ$), up to the possible development of an instability. On there other hand, for non-aligned loadings, the orientation of particles changes with the deformation, and this is expected to have a significant effect on the macroscopic behavior of the composite. For this reason, the evolution of the particle rotations will be included in the presentation of the results and associated discussions of the next section. On the other hand, the distributional ellipsoid, which is assumed to have initially the same shape and orientation as those of particles in the undeformed configuration, evolves with the macroscopic deformation, and can be easily computed, but is not expected to play a major role and will therefore not be discussed further here.

Onset of macroscopic instabilities. Theoretical results [6] suggest that composite materials can develop macroscopic (or long wavelength) instabilities at sufficiently large deformations, even when the constituent phases are *locally* strongly elliptic. Interestingly, the TSO model, developed in Part I, was found to generate macroscopic instabilities under certain conditions which can be captured through loss of the SE condition for the effective stored-energy function. As discussed in Part I, the onset of macroscopic instabilities in the incompressible composites correspond to development of a *localized* deformation (or *shear band*) on a plane (identified by the the normal vector $\mathbf{n}_{cr}$) and in the direction $\mathbf{m}_{cr}(\perp \mathbf{n}_{cr})$. In particular, our aim is to investigate (1) whether or not the homogenized behavior of the composites loses SE for different loading/microstructure conditions, and (2) what is the associated critical stretch (denoted by $\bar{\lambda}_{cr}$) and the pair of vectors ($\mathbf{m}_{cr}$ and $\mathbf{n}_{cr}$) in case of loss of SE. For the composites under study, the local behavior of the matrix is locally strongly elliptic (models (3) and (4) are strongly elliptic for all stretches), and therefore, the loss of SE of the homogenized behavior can be related to the evolution of microstructure.

For completeness, in addition to presenting the macroscopic instability results in deformation space (given by $\bar{\lambda}_{cr}$), we also present them in stress space. To this end, we need to suitably choose the arbitrary pressure p in Eq. (7) depending on the applied macroscopic loading. For simplicity, we consider instability results in stress space only for aligned pure shear and axisymmetric shear loadings. The case of aligned pure shear loading ($\bar{\lambda}_1 = \bar{\lambda}, \bar{\lambda}_2 = 1$) can be identified with the biaxial state of stress

$$\bar{\mathbf{S}} = \bar{S}_{22}\mathbf{e}_2 \otimes \mathbf{e}_2 + \bar{S}_{33}\mathbf{e}_3 \otimes \mathbf{e}_3, \tag{13}$$

where the $\bar{S}_{ij}$ denote components of the Piola-Kirchhoff stress relative to the basis $\{\mathbf{e}_i\}$. Similarly, the case of aligned axisymmetric shear loading ($\bar{\lambda}_1 = \bar{\lambda}_2 = \bar{\lambda}$) can be associated to a uniaxial state of stress in the $\mathbf{e}_3$ direction, written as

$$\bar{\mathbf{S}} = \bar{S}_{33}\mathbf{e}_3 \otimes \mathbf{e}_3. \tag{14}$$

Accordingly, we define the *critical stress* as the stress component $\bar{S}_{33}$ at which the composite loses the strong ellipticity under these two types of loading, namely,

$$\bar{S}_{cr}^{PS} = \bar{S}_{33}(\bar{\lambda}_{cr}) = -\bar{\lambda}_{cr}^{2}\frac{\partial\widehat{\phi}^{PS}(\bar{\lambda}_{cr},0)}{\partial\bar{\lambda}}, \qquad \bar{S}_{cr}^{AS} = \bar{S}_{33}(\bar{\lambda}_{cr}) = -\frac{1}{2}\bar{\lambda}_{cr}^{3}\frac{\partial\widehat{\phi}^{AS}(\bar{\lambda}_{cr},0)}{\partial\bar{\lambda}}. \quad (15)$$

In this work, we will only be concerned with macroscopic instabilities, as just described. For other types of instabilities, the reader is referred to the work of Michel et al. [12] in the context of two-dimensional particle-reinforced composites.

As explained in Part I of this work, the calculation of the effective stored-energy function $\widehat{\phi}$, as well as of the particle rotation $\bar{\psi}^{(2)}$, requires the computation of the tensor $\mathbf{E}$, which, in turn, requires the calculation of the integrals associated with the tensors $\mathbf{P}_r$, $r = 1,2,3$ (see Appendix A of Part I). For practical reasons, we make use here of the (numerical) Gaussian quadrature integration procedure presented in Appendix B of Part I for calculating the tensors $\mathbf{P}_r$. The calculation of these integrals is the most computationally intensive part of the procedure, and a high number of Gaussian points may be needed to achieve convergence, especially when the particles have aspect ratios that are far from $w = 1$. A FORTRAN program has been written for this purpose and is available upon request. In the next section, the above-mentioned sets of results will be presented and discussed in detail.

3. Applications

In this section, we present some representative examples for the *tangent* second-order estimates for particle-reinforced elastomers with an incompressible matrix phase and (rigid) spheroidal particles undergoing macroscopic deformations of the form (5). In particular, we study the TSO estimates for particle-reinforced composites with Gent (Eq. (4)) and neo-Hookean (Eq. (3)) matrix phases. For simplicity, results for the effective energy, stress and modulus tensors are normalized by the ground-state shear modulus (that is, $\mu^{(1)} = 1$), and for the case of composites with Gent matrices, results are shown for several values of lock-up parameter J_m. We provide results for both prolate and oblate shapes of particles, and several values of the volume fraction c and particle aspect ratio w. Note that results are shown with solid and dotted lines up to the point at which the effective incremental modulus tensor loses strong ellipticity, beyond which the results are depicted by dashed and dashed-dotted lines, respectively. For the cases when no loss of SE is detected, they are truncated at some sufficiently large strain. In this connection, the circle marker '•' in the plots is used to denote the point at which loss of SE first takes place (as the loading parameter $\bar{\lambda}$ is increased). Moreover, in most of the figures, the results for the pure neo-Hookean matrix are included for comparison purposes.

The results provided in this section are organized as follows. First, in subsection 3.1, we address the effective behavior of particle-reinforced, neo-Hookean and Gent elastomers subjected to *aligned* loadings ($\bar{\theta} = 0^{\circ}$). Attention is devoted to (aligned) *pure shear* and *axisymmetric shear* loadings. Next, in subsection 3.2, we will present representative results for the overall behavior of particle-reinforced neo-Hookean elastomers subjected to *non-aligned* loadings ($\bar{\theta} \neq 0^{\circ}$). In this subsection, similar to the first one, attention is restricted to (non-aligned) pure and axisymmetric shear loadings. Also, in both subsections, in order to consider exclusively the impact of the particle shape on the macroscopic behavior, results are first provided for dilute concentration of particles ($c \ll 1$), followed by results for several (finite) values of c. The theoretical significance for the dilute concentration results is that they can be interpreted as a generalization of the results of Eshelby [5] for a composite material consisting of dilute concentrations of aligned, rigid spheroidal

inclusions in a nonlinear hyperelastic matrix. In fact, the nonlinear results of this paper reduce exactly to the Eshelby results in the infinitesimal (linearized) deformation regime.

3.1. *Aligned loadings*

In this subsection, we restrict our attention to the special case of macroscopically *aligned* loadings, characterized by $\bar{\theta} = 0^\circ$. It is recalled from Part I that in this case the particles do not rotate ($\bar{\psi}^{(2)} = 0^\circ$) for any applied stretch (up to the possible development of an instability). Moreover, results are given for two specific types of aligned loadings, namely, aligned *pure shear* loading and aligned *axisymmetric shear* loading. It is important to observe that for the case of aligned axisymmetric loading, the overall behavior of the composite remains transversely isotropic in the deformed configuration with the axis of symmetry aligned with the $\mathbf{e}_3$ direction. On the other hand, for the case of aligned pure shear loading, the composite is initially transversely isotropic, but develops general orthotropic overall response (whose principal axes are aligned with the $\mathbf{e}_i$ basis directions) in the deformed configuration. It is also noted that the results in this subsection will be presented as functions of the macroscopic logarithmic strain $\bar{e} = \ln(\bar{\lambda})$. Accordingly, for the case of prolate particles, the compressive (tensile) axis of loading is aligned with the longest principal axis of particles for $\bar{e} > 0$ ($\bar{e} < 0$), while the opposite is true for the case of oblate particles. This remark will be of the essence in the physical interpretation of loss of SE results provided later in this subsection.

Figure 1 presents plots for the TSO estimates for the effective stored-energy function $\widehat{\phi}_0$ of the neo-Hookean elastomers reinforced with *dilute* concentrations of particles, as defined by expressions (12). Figures 1(a) and (b) show plots for pure shear loading ($\bar{\lambda}_1 = \bar{\lambda}, \bar{\lambda}_2 = 1$), as a function of the strain $\bar{e} = \ln(\bar{\lambda})$, for the cases of prolate and oblate particles, respectively, while Fig. 1(c) and (d) show corresponding plots for axisymmetric shear loading ($\bar{\lambda}_1 = \bar{\lambda}_2 = \bar{\lambda}$). The results for prolate particles are given for aspect ratios $w = 2$, 4, and 8, and those for oblate particles are given for aspect ratios $w = 0.5$, 0.25, and 0.125. For comparison purposes, the finite element results (FEM) of Lopez-Pamies et al. [7] (obtained for a single rigid inclusion embedded in a neo-Hookean elastomer matrix), as well as the corresponding TSO results for the special case of spherical particles ($w = 1$) are also included in the plots. An immediate observation from this figure is that the aspect ratio of particles has a significant reinforcing effect on the overall response of the composite at fixed particle concentrations. We also observe that TSO estimate provides fairly good agreement with the FEM results for spherical particles (up to the point where the simulations were carried out) for both pure shear and axisymmetric shear loadings. Moreover, it is noticed from Fig. 1 that the predictions of the TSO model for the macroscopic response of the composites with spherical particles remain *macroscopically* stable for all strains, while those of the composites with prolate and oblate particles become unstable for $\bar{e} > 0$ and for $\bar{e} < 0$, respectively, under both types of loadings. We will discuss these macroscopic instabilities and the associated failure mechanisms in more detail in the context of the next two figures.

Figure 2 provides plots of the TSO estimates for the overall response of the particle-reinforced elastomer with a neo-Hookean matrix phase and particle volume fractions $c = 0.05$, 0.15, and 0.25, under *aligned pure shear* loading. Figures 2(a) and (b) show plots for the macroscopic stress measure $\bar{S}^{PS}$ as a function of the logarithmic strain $\bar{e} = \ln(\bar{\lambda})$. In particular, part (a) shows the results for spherical particles ($w = 1$) and compares them with the corresponding FEM results of Lopez-Pamies et al. [7], while part (b) shows the results for prolate and oblate shapes of particles with fixed aspect ratios $w = 4$ and $w = 0.25$, respectively. (It should be noted that the FEM results correspond to unit cell calculations containing 30 randomly positioned spherical particles.) Also, Figs. 2(c) and (d) show plots for certain shear components of the effective incremental modulus tensor $\widehat{\mathbf{L}}^c$, as

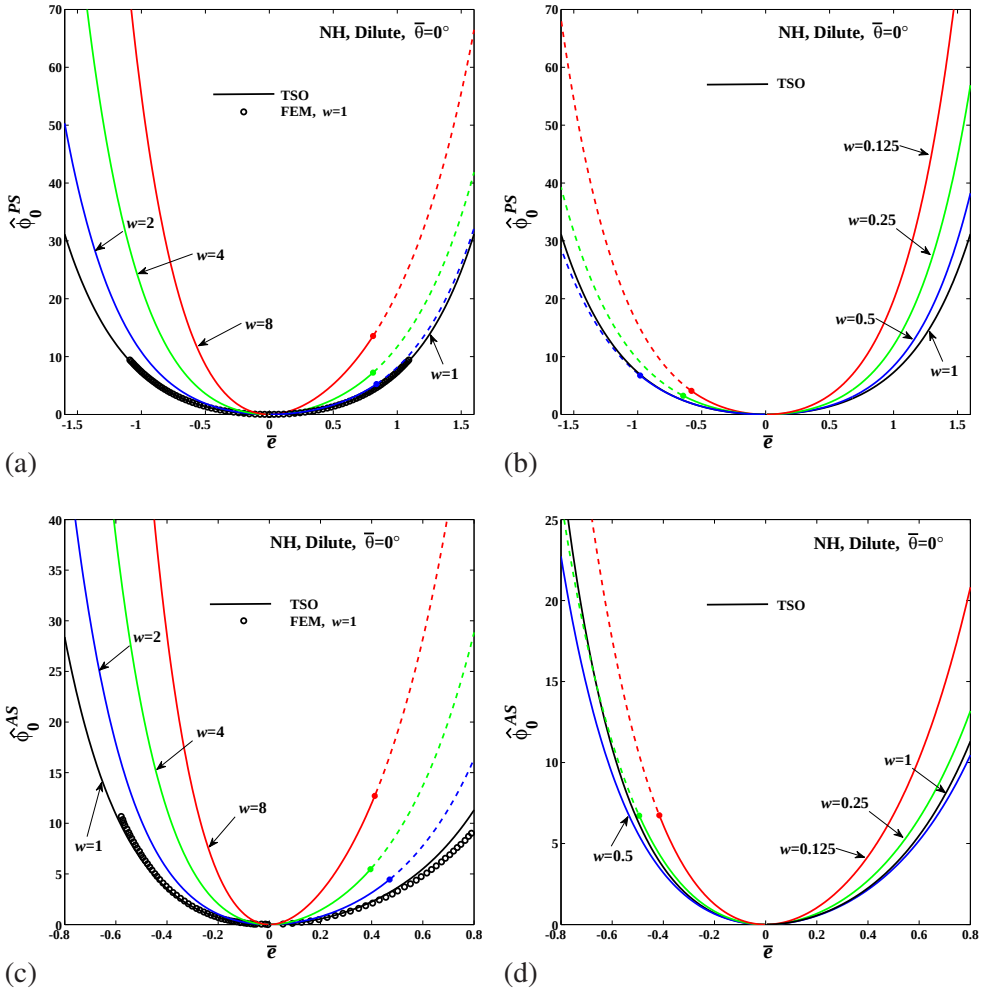

Figure 1. Tangent second-order (TSO) estimates for the effective stored-energy function $\widehat{\phi}_0(\bar{\lambda})$ of neo-Hookean elastomers reinforced with dilute concentrations of rigid particles, as functions of the macroscopic logarithmic strain $\bar{e} = \ln(\bar{\lambda})$. Two *aligned* loadings are considered: *pure shear* (PS) ($\bar{\lambda}_1 = \bar{\lambda}$, $\bar{\lambda}_2 = 1$), and *axisymmetric shear* (AS) ($\bar{\lambda}_1 = \bar{\lambda}_2 = \bar{\lambda}$). (a) Prolate particles ($w \geq 1$) under PS loading, (b) oblate particles ($w \leq 1$) under PS loading, (c) prolate particles under AS loading, and (d) oblate particles under AS loading. The finite element (FEM) results of Lopez-Pamies et al. [7] for the case of spherical particles ($w = 1$) are also included for comparison.

functions of $\bar{e} = \ln(\bar{\lambda})$, for prolate particles with $w = 4$ and oblate particles with $w = 0.25$, respectively. The main observation from Fig. 2(a) is that the TSO estimate provides fairly good agreement with the FEM results (up to the point where the simulations were carried out), especially for the smaller particle concentrations. For the higher volume fraction ($c = 0.25$), the TSO estimates tend to *underestimate* the FEM results at sufficiently large stretches, but are still in good agreement with the FEM results for stretches of less than $\bar{\lambda} = 1.4$. This is partially due to the fact that in this work the TSO model makes use of the Willis *lower bound* [16] for estimating the behavior of the associated linear comparison composite [3]. In addition, compared to the results for spherical particles (Fig. 2(a)), the results in Fig. 2(b) for spheroidal shapes show an enhanced reinforcing effect, which is due to the combined role of aspect ratio w and volume fraction c on the overall response of the composite. It is further observed from Fig. 2(b) that, for a fixed particle volume fraction, the composite stiffening is larger for elongated particles ($w = 4$) than for oblate particles ($w = 0.25$), as long as the composite response remains strongly elliptic. Next, we observe from Fig. 2(b) that the composites with finite concentrations of prolate and oblate particles become unstable at positive strains ($\bar{e} > 0$) and negative strains ($\bar{e} < 0$), respectively, when (for both cases) the compressive loading axis is aligned with the longest axis

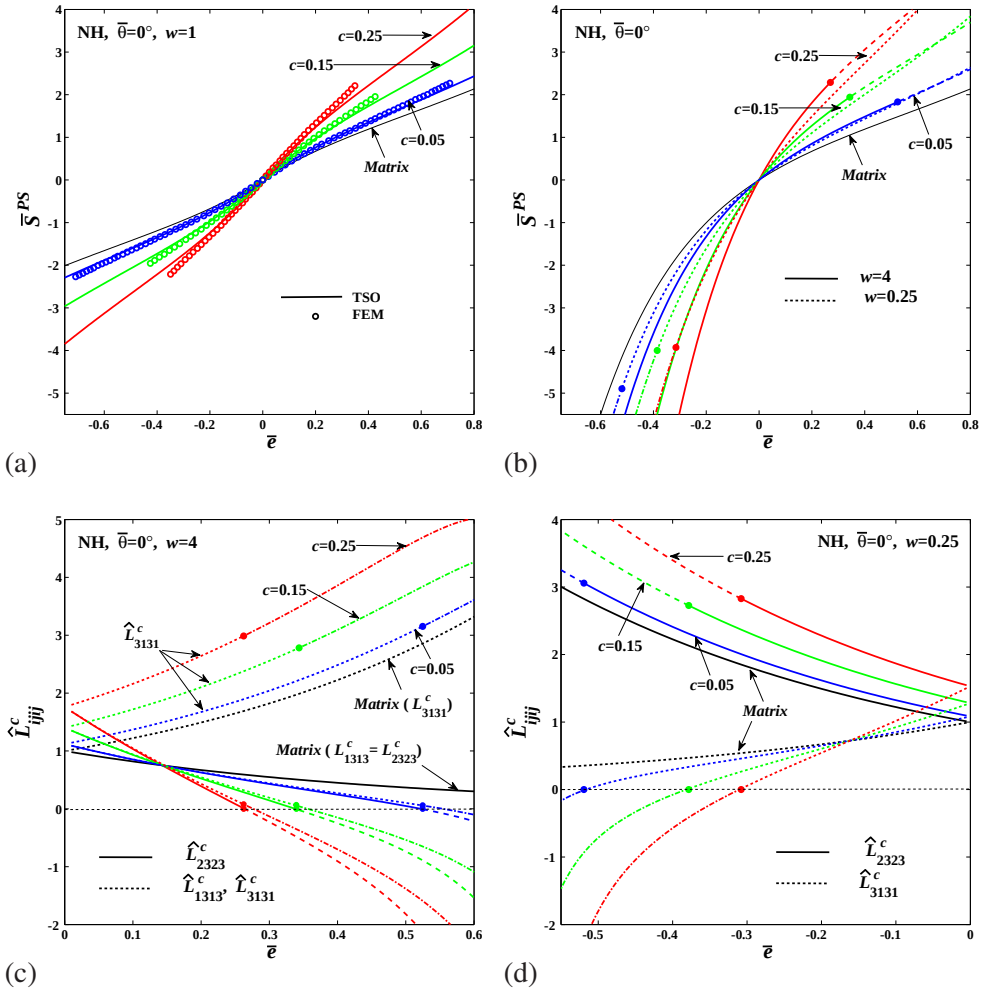

Figure 2. TSO estimates for particle-reinforced, neo-Hookean elastomers under aligned *pure shear* loading ($\bar{\lambda}_1 = \bar{\lambda}$, $\bar{\lambda}_2 = 1$), as functions of the macroscopic logarithmic strain $\bar{e} = \ln(\bar{\lambda})$. The macroscopic stress $\bar{S}^{PS}$ for: (a) spherical ($w = 1$), and (b) spheroidal ($w = 4, 0.25$) particles. Certain shear components of the effective modulus tensor $\widehat{L}^c_{ijkl}$ for: (c) prolate ($w = 4$) and (d) oblate ($w = 0.25$) particles. Results are shown for the volume fractions $c = 0.05$, 0.15 and 0.25. The finite element (FEM) results of Lopez-Pamies et al. [7] for spherical particles are also provided for comparison in part (a).

of the particles. Consistent with what was anticipated in Section 5.2 of Part I for prolate particles, it is seen from Fig. 2(c) that both the shear modulus $\widehat{L}^c_{1313}$ transverse to the long axis of the particles (and in the in-plane direction $\mathbf{e}_1$), as well as the shear modulus $\widehat{L}^c_{2323}$ transverse to the long axis of the particles (but in the out-of-plane direction $\mathbf{e}_2$) decrease with increasing tensile strain in the $\mathbf{e}_1$ direction (and, therefore, increasing compressive strain the $\mathbf{e}_3$ direction). However, in this case with a moderate volume fraction and aspect ratio ($c \leq 0.3$ and $w \leq 5$), $\widehat{L}^c_{2323}$ actually reaches zero before $\widehat{L}^c_{1313}$, and therefore the loss of ellipticity first occurs through a shear band whose normal is parallel to $\mathbf{e}_3$, and whose slip direction is along the out-of-plane direction $\mathbf{e}_2$ (i.e., out of the loading plane). On the other hand, for the case of oblate particles, the loss of SE takes place through vanishing of the shear modulus $\widehat{L}^c_{3131}$ (in the plane perpendicular to the long axis of the oblate particles, and in the direction of the loading axis $\mathbf{e}_3$). It is also observed from these figures that the reinforced elastomers lose macroscopic stability earlier for larger particle concentrations.

Similar to the previous figure, Fig. 3 provides results for the TSO estimates for the overall response of the particle-reinforced elastomers with a neo-Hookean matrix phase and particle volume fractions $c = 0.05$, 0.15, and 0.25, under *aligned axisymmetric shear* loading ($\bar{\lambda}_1 = \bar{\lambda}_2 = \bar{\lambda}$). Figures 3(a) and (b) depict the macroscopic stress measure $\bar{S}^{AS}$, as a function of the logarithmic strain $\bar{e} = \ln(\bar{\lambda})$. In particular, part (a) shows the results for

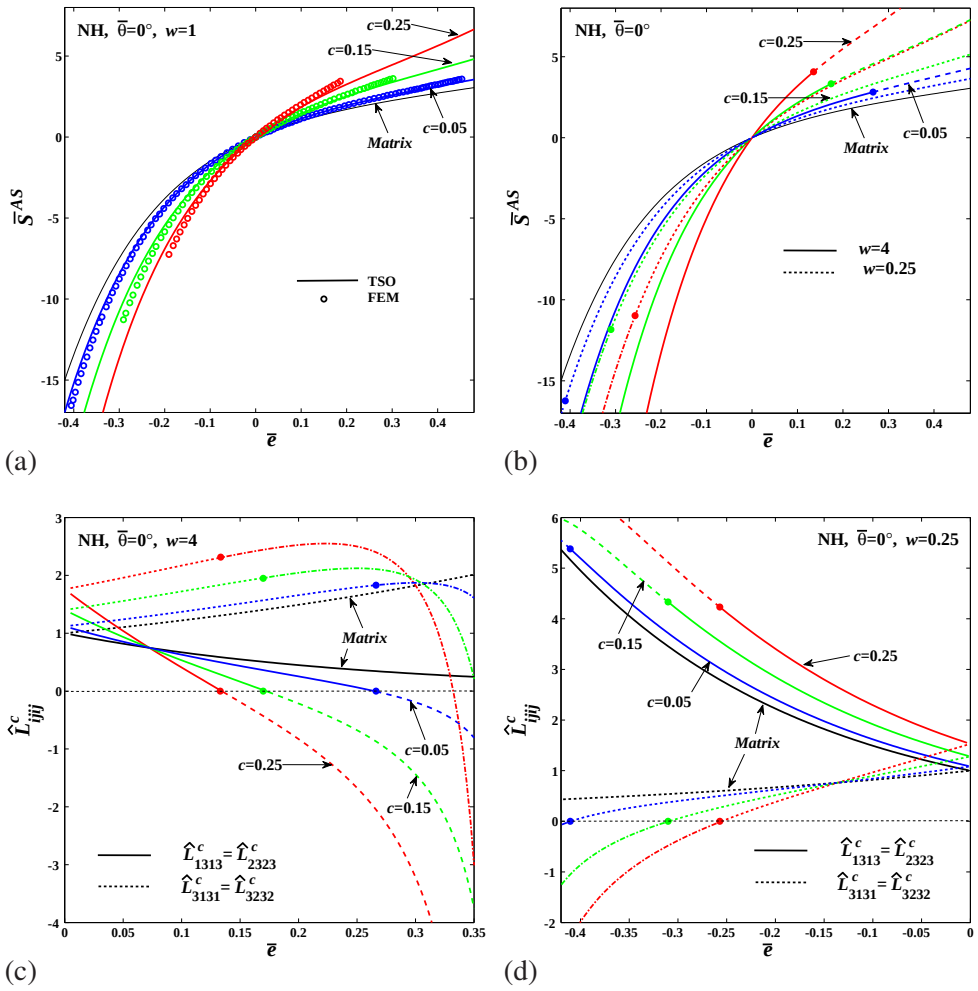

Figure 3. TSO estimates for particle-reinforced, neo-Hookean elastomers under aligned *axisymmetric shear* loading ($\bar{\lambda}_1 = \bar{\lambda}_2 = \bar{\lambda}$), as functions of the macroscopic logarithmic strain $\bar{e} = \ln(\bar{\lambda})$. The macroscopic stress $\bar{S}^{PS}$ for: (a) spherical ($w = 1$), and (b) spheroidal particles ($w = 4, 0.25$). Certain shear components of the effective modulus tensor $\widehat{L}^c_{ijkl}$ for: (c) prolate ($w = 4$), and (d) oblate ($w = 0.25$) particles. Results are shown for various volume fractions $c = 0.05$, 0.15 and 0.25. The finite element (FEM) results of Lopez-Pamies et al. [7] for the case of spherical particles are also included for comparison in part (a).

spherical particles ($w = 1$) in which the corresponding FEM results of Lopez-Pamies et al. [7] are also included for comparison purposes, while part (b) shows the results for prolate and oblate shapes of particles with fixed aspect ratios 4 and 0.25. In addition, Figs. 3(c) and (d) depict the variation of the moduli $\widehat{L}^c_{1313}$ and $\widehat{L}^c_{3131}$ versus the logarithmic strain $\bar{e} = \ln(\bar{\lambda})$ for prolate particles with aspect ratio $w = 4$ and oblate particles with aspect $w = 0.25$, respectively. Once again, we observe good agreement between the TSO estimates for spherical particles and the corresponding FEM results (up to the point where the simulations were carried out), for all three volume fractions of particles. In addition, similar to the case of pure shear loading, Fig. 3(b) shows that, at a fixed particle volume fraction, the composites exhibit stiffer responses for elongated particles ($w = 4$) than for oblate particles ($w = 0.25$). Figure 3(b) also shows that, for a fixed aspect ratio of particles (e.g., $w = 4$), the behavior of composites with spheroidal particles becomes progressively less stable—as determined by loss of SE—as the volume fraction of the particles increases. Next, consistent with the results of Part I (see relations (59) and (61)), Figs. 3(c) and (d) show that the loss of SE in the composites subjected to aligned axisymmetric shear loading takes place through vanishing of the effective incremental shear modulus in the plane perpendicular to the major axis of particles, namely, the components $\widehat{L}^c_{1313} (= \widehat{L}^c_{2323})$

and $\widehat{L}^{c}_{3131}(=\widehat{L}^{c}_{3232})$, for the cases of prolate and oblate particles, respectively.

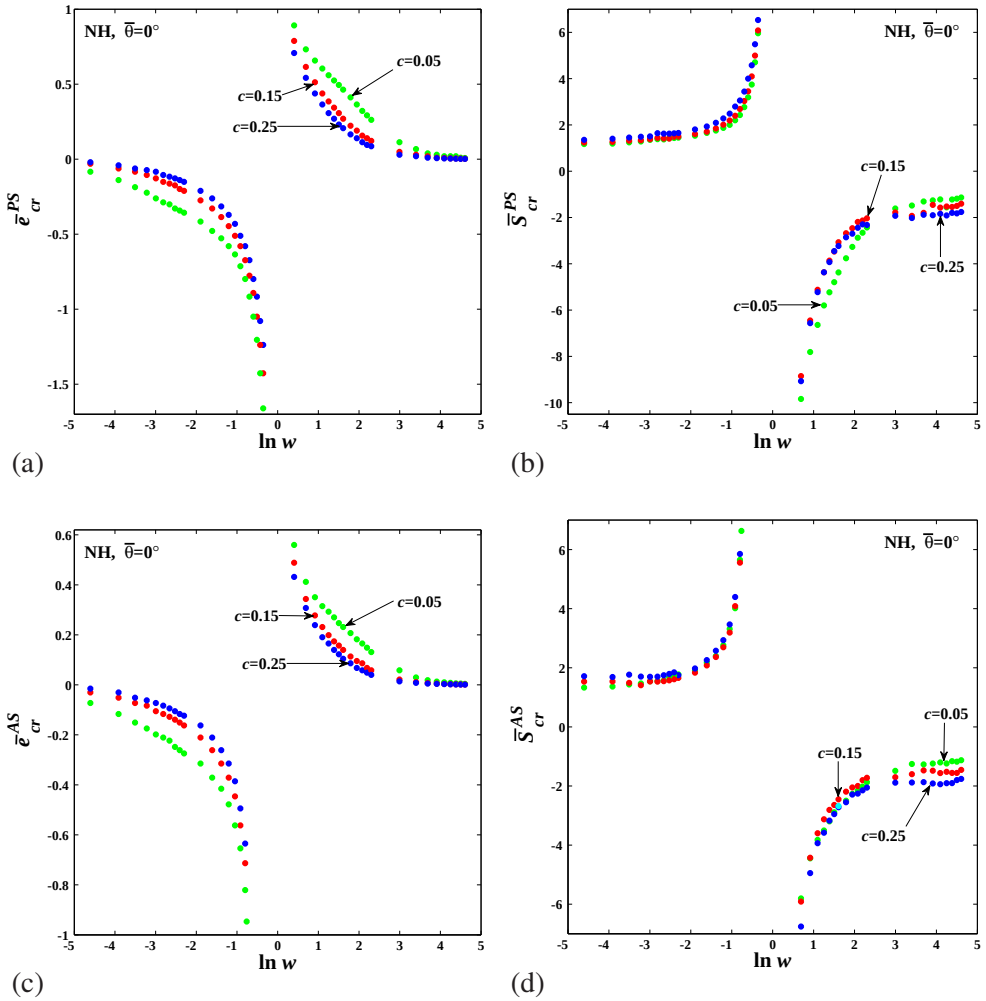

Figure 4. TSO estimates for the macroscopic instabilities (loss of SE) in particle-reinforced neo-Hookean elastomers subjected to aligned loadings. Parts (a) and (b) show *pure shear* ($\bar{\lambda}_1 = \bar{\lambda}, \bar{\lambda}_2 = 1$) results for the critical strain ($\bar{e}^{PS}_{cr}$) at which loss of SE of the homogenized elastomer takes place, and the corresponding critical stress ($\bar{S}^{PS}_{cr}$), respectively. Parts (c) and (d) show *axisymmetric shear* ($\bar{\lambda}_1 = \bar{\lambda}_2 = \bar{\lambda}$) results for the critical strain ($\bar{e}^{AS}_{cr}$) and the corresponding critical stress ($\bar{S}^{AS}_{cr}$), respectively. The results are shown for various particle concentrations as functions of the particle aspect ratio $\ln(w)$.

Figure 4 presents TSO estimates for the critical strains and stresses at which macroscopic instabilities first develop in the particle-reinforced neo-Hookean composites subjected to aligned loadings. Figures 4(a) and (b) show plots for the critical strain $\bar{e}^{PS}_{cr} = \ln(\bar{\lambda}_{cr})$ (at which the homogenized elastomer first loses SE) and the corresponding critical stress $\bar{S}^{PS}_{cr}$ (as defined in (15)), respectively, for pure shear loading. Similarly, Figs. 4(c) and (d) show plots for the critical strain ($\bar{e}^{AS}_{cr}$) and the corresponding critical stress ($\bar{S}^{AS}_{cr}$), respectively, for axisymmetric shear loading. The results are shown for several values of the concentration ($c = 0.05$, 0.15 and 0.25), as functions of the logarithm of the particle aspect ratio, $\ln(w)$. The main observation from these figures is that, for fixed volume fractions, the particle-reinforced composites become increasingly less stable in both the deformation and the stress as the value of $|\ln(w)|$ increases and the particle shape becomes progressively more prolate, or oblate. In this regard, we see from Figs. 4(a) and (c) that the critical strain curves have a vertical asymptote at $w = 1$ and horizontal asymptotes at $\bar{e}_{cr} = 0$ as $w \to \infty$ or $w \to 0$. The special case of $w = 1$ correspond to neo-Hookean elastomers reinforced by spherical (rigid) particles, which, as already mentioned, remain strongly elliptic for all deformations ($\bar{e}_{cr} \to \infty$). On the other hand, for the two extreme

values of the particle aspect ratio, namely, the limiting cases of zero and infinite aspect ratios, the composite becomes unstable at zero strain ($\bar{e}_{cr} \to 0$), which is in consistent with the fact that the composites become rigid in these two limiting cases corresponding to a laminated material with a rigid phase and a (continuous) fiber-reinforced elastomers with rigid fibers, respectively. Similar observations can be made from Fig. 4(b) and (d) for the critical stresses, except that the critical stresses tend to finite values, depending on the volume fraction of particles, in the limits as $w \to \infty$ and $w \to 0$.

In connection with this last observation, it is relevant to recall that Agoras et al. [2] derived the following results for the critical stress in composites consisting of a generalized neo-Hookean matrix and isotropic distributions of aligned, rigid, circular fibers, namely,

$$\bar{S}^{PS}_{cr} = \bar{S}^{AS}_{cr} = -\frac{1+c}{1-c}\,\mu^{(1)}. \tag{16}$$

Similarly, making use of the results provided in Appendix A of the paper [2] for the laminate composites consisting of alternating layers of incompressible neo-Hookean materials, it can be shown that the critical stress in the limit as one phase becomes rigid is given by

$$\bar{S}^{PS}_{cr} = \bar{S}^{AS}_{cr} = \frac{1}{1-c}\,\mu^{(1)}. \tag{17}$$

Moreover, note that relations (16) and (17) are valid for both *pure shear* and *axisymmetric shear* loadings. Thus, we can check from Fig. 4(b) and (d) that the trends in the results predicted by the TSO model for the critical stress are consistent with the corresponding results calculated form expressions (16) and (17), respectively, in the limiting cases of $w \to \infty$ and $w \to 0$.

Next, in Fig. 5, we investigate the influence of the matrix constitutive behavior on the macroscopic stress-strain response of the composite elastomers, when subjected to aligned pure shear (PS) and axisymmetric shear (AS) loadings. Thus, Figs. 5(a) and (b) provide plots of the macroscopic stress $\bar{S}^{PS}$ for prolate particles with $w = 4$ and oblate particles with $w = 0.25$, respectively, while Figs. 5(c) and (d) provide corresponding plots for the macroscopic stress $\bar{S}^{AS}$. In each figure, the volume fraction of particles is assumed to be fixed at $c = 0.25$, and results are shown for several values of the matrix lock-up parameters ($J_m = 50, 100$, and ∞). It is recalled that the case $J_m \to \infty$ corresponds to an incompressible neo-Hookean matrix. We observe from these figures that the composites with prolate particles tend to stiffen more significantly for compressive strains ($\bar{e} < 0$), resulting in tensile strains in the long fiber direction, while the composites with oblate particles tend to stiffen more significantly for tensile strains ($\bar{e} > 0$), corresponding to compressive strains along the short fiber direction. In addition, the amount of stiffening is more significant for larger values of J_m, as expected. Moreover, it can be shown that, the effective lock-up strain[1] for the composite materials with spheroidal particles under aligned loadings is independent of the shape of the particle and is completely determined by the values of J_m, and c. Therefore, the relations (142) in [3] for the composites with spherical particles, can be used to determine the lock-up stretch for the class of composites of interest here when subjected to aligned pure and axisymmetric shear loadings. Furthermore, the plots in Fig. 5 illustrate that, although the strain-locking parameter J_m in the Gent elastomers can have a strong influence on the macroscopic response of the reinforced elastomer, it has basically no effect on the loss of SE for the particle-reinforced composites. This is consistent with earlier findings by Lopez-Pamies and Ponte Castañeda [8] and Agoras et al. [2] that the development of macroscopic instabilities in (long) fiber-reinforced composites with

[1]The strain at which the composite locks up because of lock up in the elastomeric matrix phase

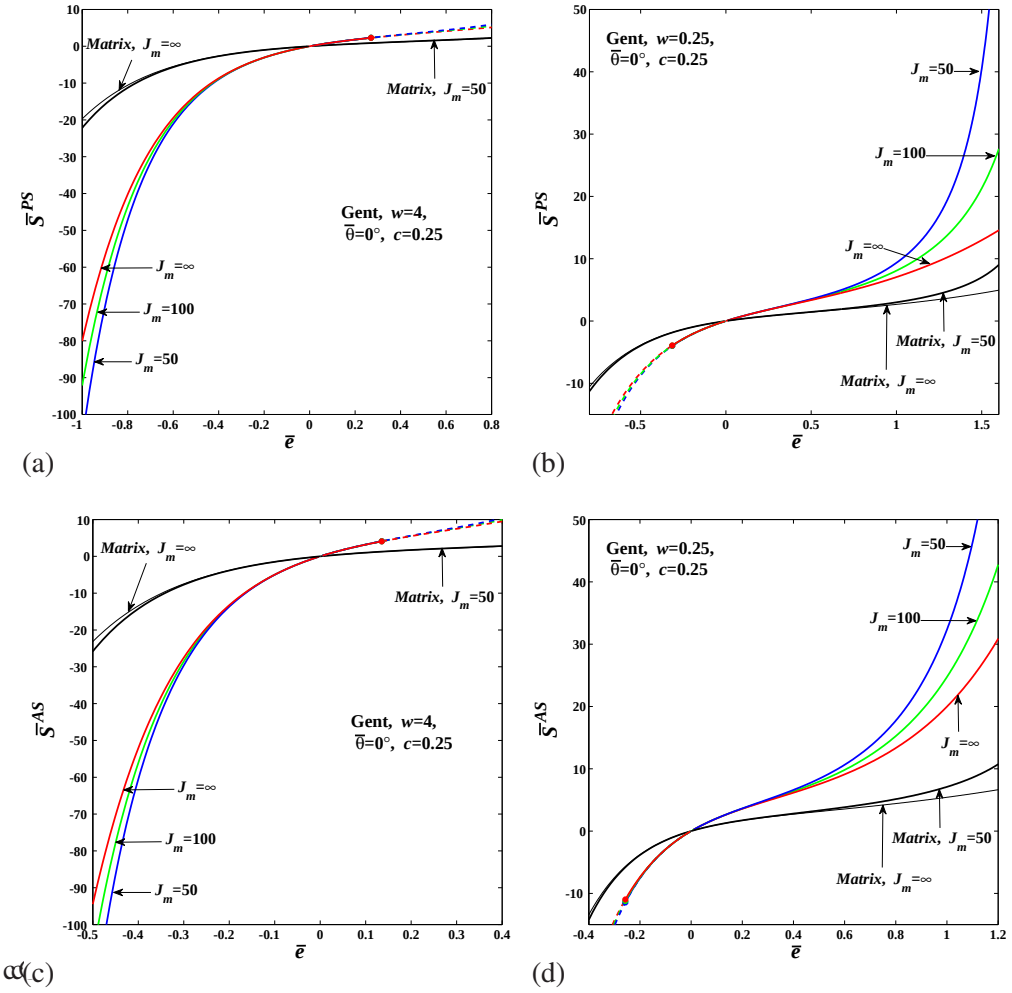

Figure 5. TSO estimates for the macroscopic stress $\bar{S}$ versus the macroscopic logarithmic strain $\bar{e} = \ln(\bar{\lambda})$ for particle-reinforced Gent elastomers. The results are shown for three values of the matrix inextensibility parameter $J_m = 50$, 100, and ∞. Four different cases are considered: (a) aligned pure shear for a prolate spheroidal shape ($w = 4$), (b) aligned pure shear for an oblate shape ($w = 0.25$), (c) aligned axisymmetric shear for a prolate shape ($w = 4$), and (d) aligned axisymmetric shear for an oblate shape ($w = 0.25$).

Gent matrix materials subjected to 2-D and 3-D loadings becomes independent of J_m for very stiff fibers.

Finally, Fig. 6 provides results for the transverse effective response of a (2-D) composite consisting of an incompressible, neo-Hookean matrix reinforced by rigid, aligned, cylindrical fibers with elliptical cross section of aspect ratio w, which are subjected to pure shear aligned with the principal axes of the elliptical fibers. The response of this type of composite to pure shear loading has also been studied in [8] and [3]. These results are compared with the corresponding results of this paper for the (3-D) neo-Hookean elastomers reinforced with aligned, spheroidal particles with the same aspect ratio w that are subjected to the same pure shear loading, but this time in a plane including the long axis of the fibers. (It should be noted here that the results for the 2-D composite with aspect ratio $w = 1$ also correspond to the transverse shear response of the 3-D composite with aspect ratio $w \to \infty$.) More specifically, Fig. 6 shows results for the effective stress $\bar{S}^{PS}$ versus the logarithmic strain $\bar{e} = \ln(\bar{\lambda})$ in 2-D and 3-D composites with fiber/particle aspect ratios $w = 1$ and $w = 4$, at the fixed fiber/particle concentration $c = 0.3$. From this figure, we first observe that the response curves for the 2-D and 3-D composites with aspect ratio $w = 1$ are fairly similar, with the spherical particles producing a slightly stiffer response. On the other hand, the responses for the 2-D and 3-D composites with aspect

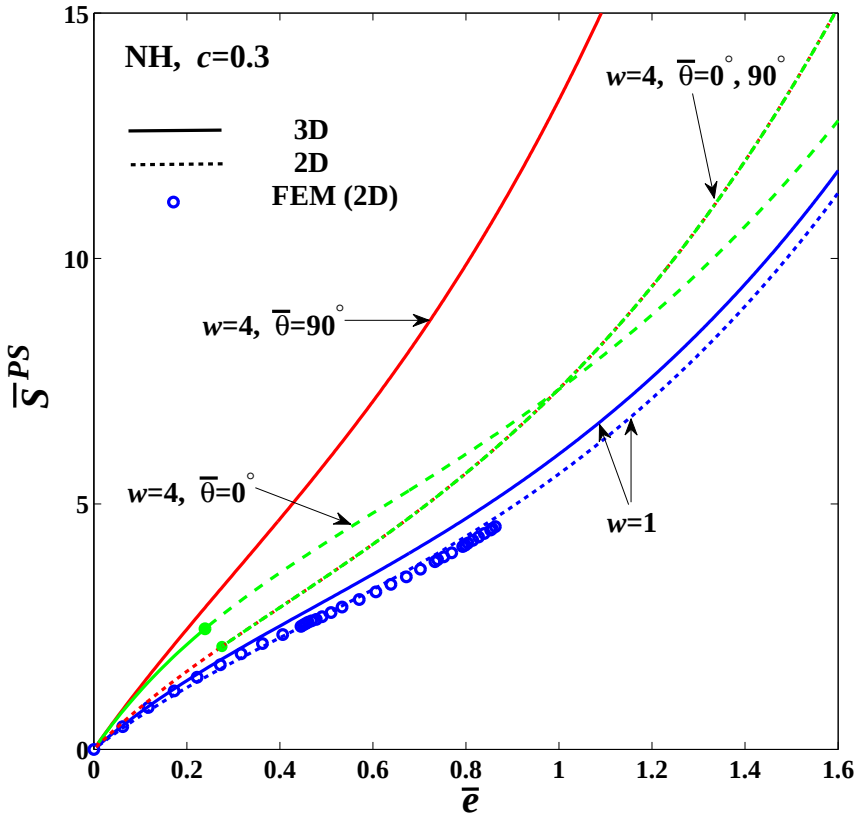

Figure 6. Comparison between the TSO estimates for the macroscopic stress $\bar{S}^{PS}$ in 2-D and 3-D rigidly reinforced elastomers subjected to aligned *pure shear* loadings. The 2-D composite is a fiber-reinforced composite which consists of an incompressible neo-Hookean matrix and a random distribution of long, aligned (rigid) fibers with elliptical cross section, and is subjected to aligned pure shear loading. The 3-D composite is the composite studied in this work with a neo-Hookean matrix and spheroidal particles, and is subjected to aligned pure shear deformation ($\bar{\lambda}_1 = \bar{\lambda}, \bar{\lambda}_2 = 1$). The results are shown as functions of the logarithmic strain $\bar{e} = \ln(\bar{\lambda})$ for two fiber/particle aspect ratios ($w = 1$ and $w = 4$), at the fixed fiber/particle concentration $c = 0.3$. The FE simulations of Moraleda et al. [13] for a 2-D fiber-reinforced composite with circular fibers ($w = 1$) are also included for comparison.

ratio $w = 4$ are quite different. While the response of the 2-D composites is the same regardless of whether the extension axis is aligned with the long particle axis ($\bar{\theta} = 90°$) or perpendicular to it ($\bar{\theta} = 0°$), the response of the 3-D composites is quite a bit stiffer when the extension axis is aligned with the long particle axis than when it is perpendicular to it. (Recall that the unstable branches of the solutions for $\bar{\theta} = 0°$ are shown in dashed and dashed-dotted lines.) However, the results for aspect ratio $w = 4$ and loading angle $\bar{\theta} = 0°$ indicate that the 2-D fiber-reinforced composites are slightly more stable than the 3-D composites with the same aspect ratio. In addition, we observe that the TSO estimate for the 2-D composite with circular fibers is in excellent agreement with the FEM simulations of Moraleda et al. [13] for the same problem (at least for the range of stretches that were achieved in the numerical simulations). In this connection, it is important to recall that the modification of the TSO estimates proposed in Part I of this work (in terms of expression (22) instead of the corresponding expression (113) in [3] involving a log term in the determinant) is free from the "geometric lock up" condition, and is much closer to the FEM results than the earlier estimate in [3], which were found to blow up for a sufficiently small value of the stretch $\bar{\lambda}$ (at $\bar{\lambda} = 1/c$, for the results shown in the plots).

3.2. *Non-aligned loadings*

In the previous subsection, we restricted our attention to cases in which the principal axes of loading are aligned with those of the particles. In this subsection, we present results for the more general case of macroscopically *non-aligned* loadings of the form (5). The idea behind presenting these results is to explore the effect of the evolution of the microstructure (here, the particle rotation) on the macroscopic response and stability of the reinforced elastomers. Keeping in mind the transverse isotropy of the reinforced elastomers of interest in this work, it will suffice to restrict our attention to loading orientation angles in the range $0 \leq \bar{\theta} \leq \pi/2$. Thus, in this section, results will be provided for variety of loading angles in this range, including $\bar{\theta} = 0^{\circ}$ and $\bar{\theta} = 0^{+\circ}$. The latter corresponds to the case in which the principal axes of loading has a very small misorientation with respect to the principal axes of the particles in the undeformed configuration. The significance of this choice will be expounded upon in the discussion below. It is also noted that all results in this subsection are for composites with neo-Hookean matrix phases of the form (3). Moreover, results are given for two specific types of *non-aligned* loadings: (1) *pure shear* at an angle, characterized by the choice $\bar{\lambda}_1 = \bar{\lambda}$, $\bar{\lambda}_2 = 1$ (in expression (5)), and (2) *axisymmetric shear* at an angle, characterized by the choices $\bar{\lambda}_1 = \bar{\lambda}_2 = \bar{\lambda}$. It is relevant to note that the transformations $\bar{\lambda} \rightarrow \bar{\lambda}^{-1}$ and $\bar{\theta} \rightarrow \bar{\theta} + \pi/2$ lead to the same pure shear loading loading. In addition, it is recalled from the formulation in Part I that the loading angle $\bar{\theta} = \bar{\theta}_2$ corresponds to rotation of the principal loading axes about the (fixed) laboratory axis $\mathbf{e}_2$, while the loading angle $\bar{\theta}_1$ (which has thus far been assumed to be zero) corresponds to a rotation of the principal loading axes about the axis $\mathbf{e}_1$. As will be seen below in the context of Fig. 7 for pure shear loading conditions, we will also consider small out-of-plane misalignments ($\bar{\theta}_1 = 0^{+\circ}$) for reasons that will become evident in the discussion of said figure. Furthermore, we note that the sign convention for the angle $\bar{\psi}^{(2)}$, characterizing the average rotation of the particles, is given by the usual right-hand rule (with respect to the fixed frame of reference, see Fig. 3a in Part I). Finally, we note that, similar to the previous subsection, we first consider the case of dilute concentrations of particles ($c \ll 1$) in order to isolate the influence of the particle shape on the macroscopic behavior and the microstructure evolution under non-aligned loadings. After doing this, we will provide results for finite concentrations of particles.

Figure 7 provides results for the TSO estimates for the effective response of a neo-Hookean elastomer reinforced with prolate particles under pure and axisymmetric shear, at the fixed loadings angles $\bar{\theta} = 0^{\circ}, 0^{+\circ}, 5^{\circ}, 45^{\circ}, 70^{\circ}$ (as well as for the angle $\bar{\theta}_1 = 0^{+\circ}$, for pure shear only). Results are shown for the fixed aspect ratio $w = 2$ and a dilute concentration of particles, as functions of the macroscopic logarithmic strain $\bar{e} = \ln(\bar{\lambda})$. Figures 7(a) and (b) show plots for the macroscopic stress $\bar{S}_0^{PS}$ and the particle rotation $\bar{\psi}^{(2)}$, respectively, for pure shear. Similarly, Figs. 7(c) and (d) show corresponding plots for axisymmetric shear. Recalling that $\bar{S}_0^{PS}$ and $\bar{S}_0^{AS}$, as determined by expressions (9) and (11), are measures of the normal stress differences defined by the loading direction, we observe from Figs. 7(a) and (c) that $\bar{S}_0^{PS}$ and $\bar{S}_0^{AS}$ are both quite sensitive to the loading angle $\bar{\theta}$. While this is to be expected for small strains, it is interesting to note that, at finite strains, the particle rotations can have significant additional effects relative to the perfectly aligned case ($\bar{\theta} = \bar{\theta}_2 = 0^{\circ}$). Indeed, it can be seen that the large rotations that are produced for the cases where the long axes of the particles are nearly (but not exactly) orthogonal to the tensile loading axis ($\bar{\theta} = 0^{+\circ}, 5^{\circ}$; $\bar{\theta}_1 = 0^{+\circ}$) are associated with significant softening relative to the perfectly aligned case ($\bar{\theta} = 0^{\circ}$), especially for axisymmetric shear. In fact, the softening is so significant that loss of ellipticity is observed for these cases (as well as for the perfectly aligned case). In connection with the particle rotations shown in Figs. 7(b) and (d), it should be noted that, when the composite is subjected to non-aligned loadings, the particles tend to align their longest axis with the tensile loading direction as the deformation progresses, implying that $\bar{\psi}^{(2)} \rightarrow \bar{\theta} - 90^{\circ}$ for $\bar{e} >> 0$, and $\bar{\psi}^{(2)} \rightarrow \bar{\theta}$ for

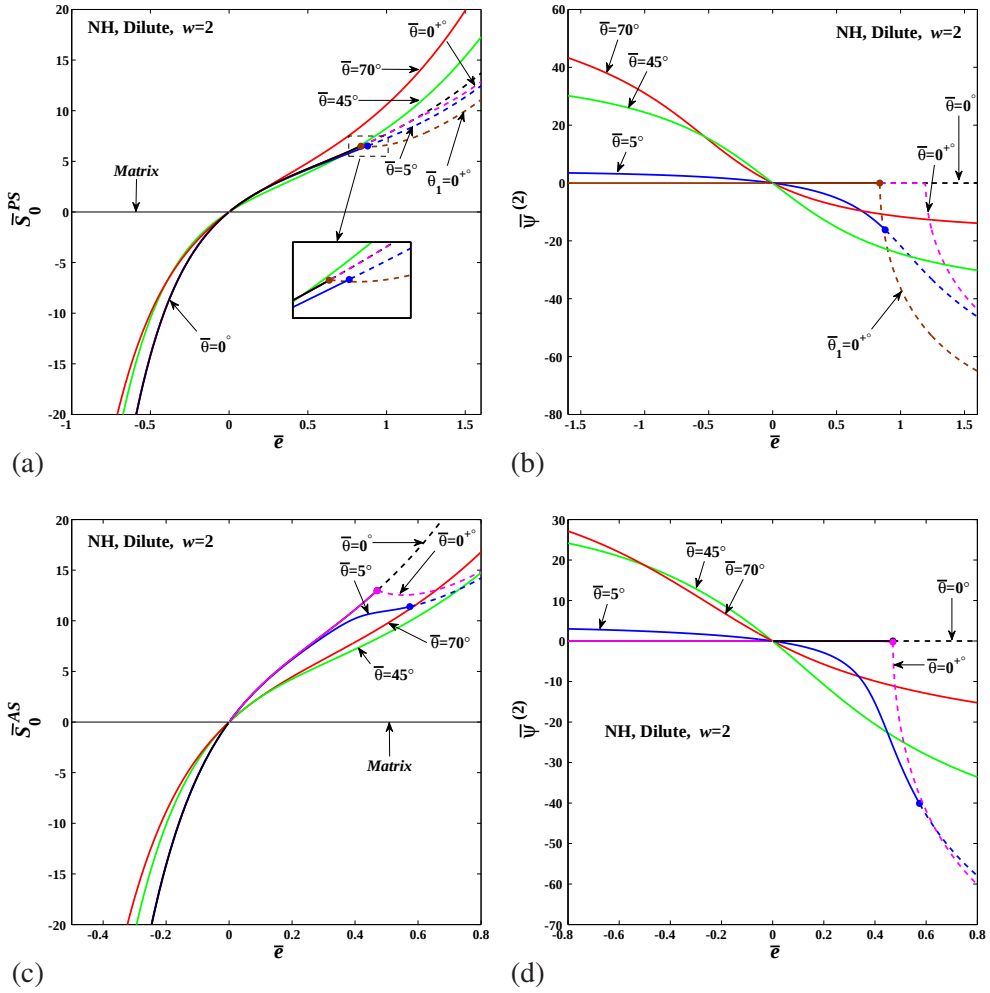

Figure 7. TSO estimates for a particle-reinforced neo-Hookean composite with a dilute concentration of *prolate* particles with aspect ratio $w = 2$ subjected to *non-aligned* loadings. Parts (a) and (b) show results for *pure shear* loading ($\bar{\lambda}_1 = \bar{\lambda}, \bar{\lambda}_2 = 1$) for the effective stress $\bar{S}_0^{PS}$ and the angle of rotation of the particles $\bar{\psi}^{(2)}$, respectively. Parts (c) and (d) show results for *axisymmetric shear* loading ($\bar{\lambda}_1 = \bar{\lambda}_2 = \bar{\lambda}$) for the effective stress $\bar{S}_0^{AS}$ and the rotation $\bar{\psi}^{(2)}$, respectively. The results are shown for various angles $\bar{\theta}$ (as well as for the out-of-plane misalignment angle $\bar{\theta}_1 = 0^{+\circ}$ for the case of pure shear lading), as functions of the macroscopic logarithmic strain $\bar{e} = \ln(\bar{\lambda})$.

$\bar{e} << 0$ (except for $\bar{\theta} = 0, \pi/2$, for which, the particles do not rotate and $\bar{\psi}^{(2)} = 0^\circ$). For example, for the loading angle $\bar{\theta} = 70^\circ$, $\bar{\psi}^{(2)}$ tends to the values -20° and 70° for $\bar{e} > 0$ and $\bar{e} < 0$, respectively.

At this point, it is useful to explore in more detail the possible connections between the particle rotations and the loss of SE condition. For this purpose, we show in Fig. 8 the appropriate shear components of the incremental modulus tensor for neo-Hookean elastomers reinforced with *dilute* concentrations of prolate particles with $w = 2$, subjected to aligned loading conditions. Thus, we observe from Fig. 8(a) that for *pure shear* loading conditions both $\widehat{L}^c_{1313}$ and $\widehat{L}^c_{2323}$ decrease with increasing strain and actually vanish, but at different levels of the applied strain $\bar{e}$. (Note that the corresponding moduli $\widehat{L}^c_{3131}$ and $\widehat{L}^c_{3232}$ also vanish at the appropriate strains, but have very different behaviors tending to increase or remain constant before vanishing.) On the other hand, we see from Fig. 8(b) for *axisymmetric shear* loading conditions that $\widehat{L}^c_{1313}$ and $\widehat{L}^c_{2323}$ are identical by symmetry and vanish at the same applied strain. ($\widehat{L}^c_{3131}$ and $\widehat{L}^c_{3232}$ also vanish but exhibit different trends.) In addition, it is noted that vanishing of $\widehat{L}^c_{1313}$ implies that the particles can rotate freely about the $\mathbf{e}_2$ axis (in the $\mathbf{e}_1 - \mathbf{e}_3$ plane), while vanishing of $\widehat{L}^c_{2323}$ allows the particles

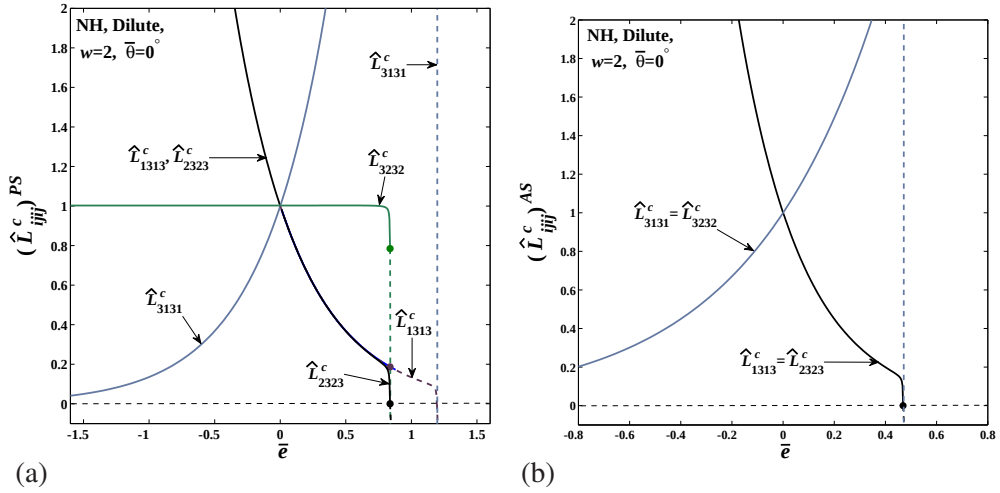

Figure 8. TSO estimates for the incremental shear moduli of particle-reinforced neo-Hookean composites with a dilute concentration of *prolate* particles with aspect ratio $w = 2$ subjected to *aligned* loadings. (a) Results for *pure shear* loading ($\bar{\lambda}_1 = \bar{\lambda}, \bar{\lambda}_2 = 1$). (b) Results for *axisymmetric shear* loading ($\bar{\lambda}_1 = \bar{\lambda}_2 = \bar{\lambda}$).

to rotate freely about the $\mathbf{e}_1$ axis (in the $\mathbf{e}_2 - \mathbf{e}_3$ plane). Moreover, the onset of the sudden rotations observed in Figs. 7(b) and (d) for pure shear and axisymmetric shear loading conditions, respectively, are found to coincide precisely with the vanishing of the corresponding incremental moduli (as shown in Figs. 8(a) and (b)). Thus, for pure shear, $\widehat{L}^c_{1313}$ and $\widehat{L}^c_{2323}$ vanish at different levels of the applied strain $\bar{e}$, and the particles can be seen to start rotating about the $\mathbf{e}_2$ and $\mathbf{e}_1$ axes, respectively, at the corresponding values of the applied strain $\bar{e}$. In this case, the loss of SE is associated with the first modulus to vanish (in this case, $\widehat{L}^c_{2323}$, corresponding to rotation of the particles out of the loading plane). On the other hand, for the case of axisymmetric shear, $\widehat{L}^c_{1313} = \widehat{L}^c_{2323}$, and the particles can start rotating about any axis in the $\mathbf{e}_1$-$\mathbf{e}_2$ plane (because of the symmetry) at the same value of the applied strain $\bar{e}$. In conclusion, it can be seen that the sudden rotation—or *flopping*—of the fibers can be linked directly to the loss of ellipticity of the incremental elasticity tensor of the composites (at least for dilute concentrations).

Figure 9 provides results for the TSO estimates for the effective response of a neo-Hookean elastomer reinforced with oblate particles, under pure and axisymmetric shear loadings at the fixed loadings angles, $\bar{\theta} = 0, 0^{+\circ}5^\circ, 45^\circ, 70^\circ$. Results are shown for the fixed aspect ratio $w = 0.5$, and a dilute concentration of particles, as functions of the macroscopic logarithmic strain $\bar{e} = \ln(\bar{\lambda})$. Figures 9(a) and (b) show plots for the macroscopic stress $\bar{S}^{PS}_0$ and the rotation of the particles $\bar{\psi}^{(2)}$, respectively, for pure shear. Similarly, Figs. 9(c) and (d) show corresponding plots for axisymmetric shear. As discussed in the context of the previous figure for the prolate particles, the results of Fig. 9 put into evidence the significant influence of the rotation of the particles on the effective response and macroscopic stability of the particle-reinforced composites subjected to pure and axisymmetric shear loadings. However, there are important differences between the oblate and prolate particle cases. Thus, we observe from Fig. 9(a) that the most significant softening in the macroscopic stress-strain relation, as well as the associated loss of strong ellipticity, occur for compressive applied strains ($\bar{e} < 0$), in contrast with the prolate-particles composites (where the most pronounced softening and associated instabilities take place for tensile strains). In particular, Fig. 9(a) shows that, when a slightly misaligned pure shear ($\bar{\theta} = 0^{+\circ}$) is applied, a burst of softening occurs starting at a certain negative value of the critical strain $\bar{e}_{cr}$, which, as mentioned earlier, is concurrent with the large particle rotations observed in Fig. 9(b). As also discussed earlier in the context of the composites with prolate particles, this is entirely consistent with the development of flopping-type instability at the critical strain $\bar{e}_{cr}$. This softening, however, becomes less pronounced with

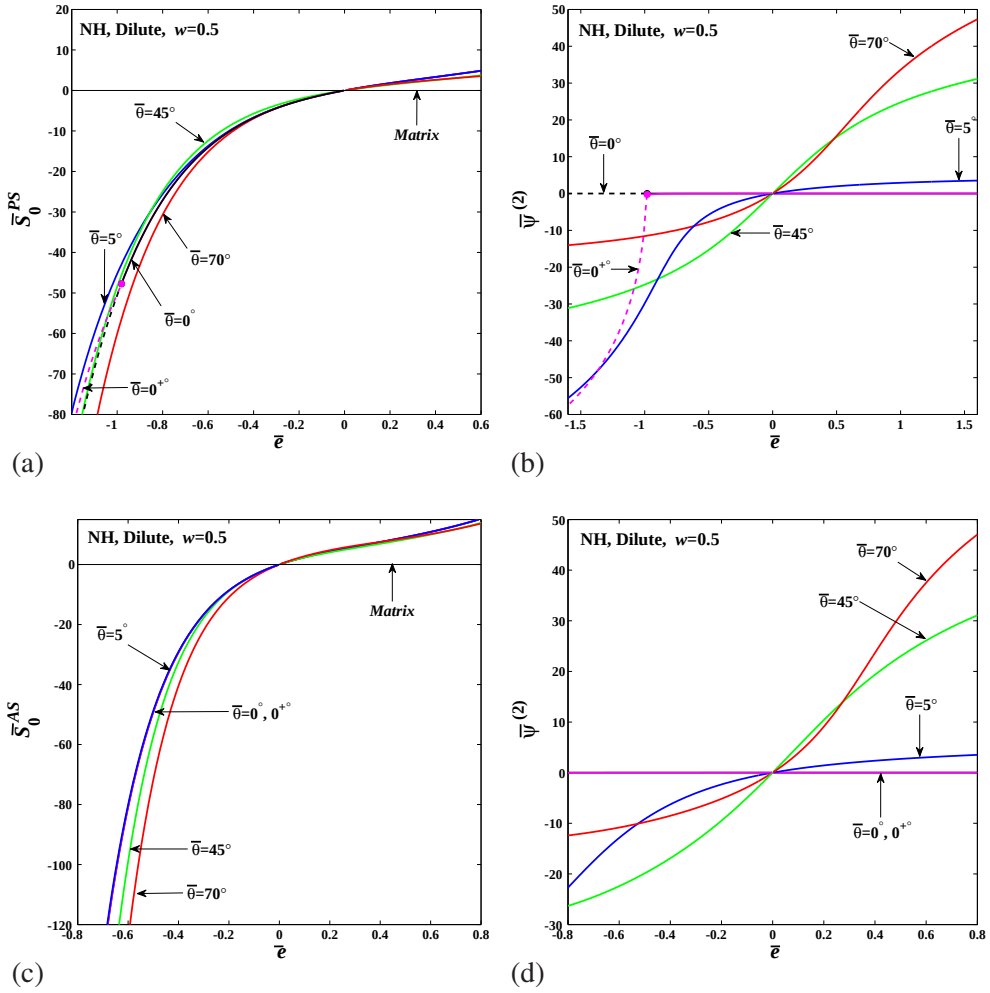

Figure 9. TSO estimates for a particle-reinforced neo-Hookean composite with a dilute concentration of *oblate* particles with aspect ratio $w = 0.5$ subjected to *non-aligned* loadings. Parts (a) and (b) show results for *pure shear* loading ($\bar{\lambda}_1 = \bar{\lambda}, \bar{\lambda}_2 = 1$) for the effective stress $\bar{S}_0^{PS}$ and the angle of rotation of the particles $\bar{\psi}^{(2)}$, respectively. Parts (c) and (d) show results for *axisymmetric shear* loading ($\bar{\lambda}_1 = \bar{\lambda}_2 = \bar{\lambda}$) for the effective stress $\bar{S}_0^{AS}$ and the rotation $\bar{\psi}^{(2)}$, respectively. The results are shown for various angles $\bar{\theta}$, as functions of the macroscopic logarithmic strain $\bar{e} = \ln(\bar{\lambda})$.

increasing loading angle $\bar{\theta}$, due to the fact that the oblate particles will rotate more slowly and thus accommodate a smaller portion of the macroscopic compressive strain for such larger values of $\bar{\theta}$. On the contrary, when the composite is subjected to tensile strains ($\bar{e} > 0$), no *softening* phenomenon is observed (for the chosen loading angles), and the composite exhibits a consistently stiffer response for smaller loading angles, once again, due to the fact that the oblate particles rotate slower at a smaller $\bar{\theta}$ for tensile strains. On the other hand, as seen in Fig. 9(c), no loss of ellipticity is detected for the composites under axisymmetric loading, in agreement with the results in Fig. 1(d) for the case of $w = 0.5$. The composites, nevertheless, show a systematically softer behavior in compression ($\bar{e} < 0$) when the particles undergo a faster and larger rotation. Finally, similar to the case of prolate particles, we observe from Fig. 9 (b) and (d) that oblate particles also tend to align (one of) their major axes with the tensile direction of the non-aligned loading as the deformation increases, and thus we deduce that in this case $\bar{\psi}^{(2)} \to \bar{\theta}$ at $\bar{e} >> 0$, and $\bar{\psi}^{(2)} \to \bar{\theta} - 90^\circ$ at $\bar{e} << 0$ (except for $\bar{\theta} = 0^\circ, \pi/2$, when the particles do not rotate).

Figure 10 presents results for the TSO estimates for the effective response of incompressible, neo-Hookean elastomers reinforced with rigid particles in dilute concentrations, subjected to non-aligned pure and axisymmetric shear loadings at a fixed angle $\bar{\theta} = 25^\circ$. Results are shown for prolate particles with aspect ratios 1, 1.1, 2, 4 and 8, as functions

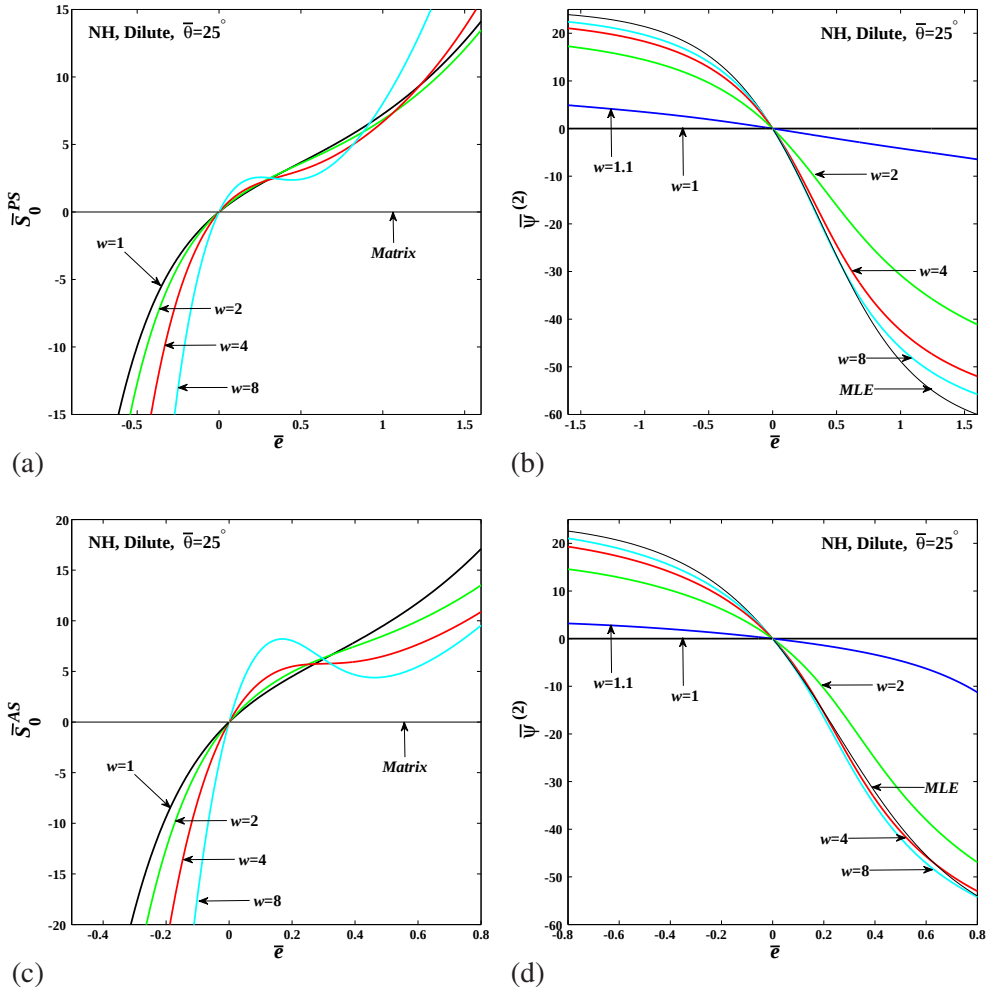

Figure 10. TSO estimates for particle-reinforced neo-Hookean composites with dilute concentrations of *prolate* particles subjected to *non-aligned* loadings at the fixed angle $\bar{\theta} = 25°$. Parts (a) and (b) show results for the effective stress $\bar{S}_0^{PS}$ and the angle of rotation of the particles $\bar{\psi}^{(2)}$, respectively, for *pure shear* loading ($\bar{\lambda}_1 = \bar{\lambda}, \bar{\lambda}_2 = 1$). Parts (c) and (d) show results for the effective stress $\bar{S}_0^{AS}$ and the rotation $\bar{\psi}^{(2)}$, respectively, for *axisymmetric shear* ($\bar{\lambda}_1 = \bar{\lambda}_2 = \bar{\lambda}$). The results are shown for particle aspect ratios $w = 1, 1.1, 2, 4, 8$, as functions of the macroscopic logarithmic strain $\bar{e} = \ln(\bar{\lambda})$.

of the macroscopic logarithmic strain $\bar{e} = \ln(\bar{\lambda})$. Figures 10(a) and (b) show plots for the case of pure shear loading for the macroscopic stress $\bar{S}_0^{PS}$ and the rotation of the particles $\bar{\psi}^{(2)}$, respectively. Similarly, Figs. 10(c) and (d) show corresponding plots for the case of axisymmetric shear loading. It can be seen from Fig. 10(a) and (c) that the effective stress-strain plots (for pure and axisymmetric shear loadings) exhibit a *softening* effect for tensile strains ($\bar{e} > 0$), which gets progressively more significant with increasing aspect ratio w. As discussed earlier, this effect is linked to the associated evolution of the microstructure. In fact, for non-aligned loadings, the finite rotation of rigid particles (see Figs. 10(b) and (d)) serves to *accommodate* some part of the total macroscopic deformation, so that smaller strains are produced in the elastomeric matrix phase. Interestingly, the largest particle rotations corresponding to the largest aspect ratios can be correlated with the strongest softening in the macroscopic stress-strain relations, for both pure and axisymmetric shear loadings. It also should be remarked that, at the chosen loading angle ($\bar{\theta} = 25°$), no loss of SE is detected for either loading conditions. The reason behind this, as mentioned earlier, is that, at this relatively large value of $\bar{\theta}$, the compression along the major axis of particles never reaches the level required for loss of SE to occur.

In addition, consistent with earlier observations, it can be seen from Figs. 10(b) and (d)

that the particles tend to align themselves with the tensile loading axis, so that the average rotation of the particles for this particular loading angle ($\bar{\theta} = 25^\circ$) exhibits the asymptotic behaviors: $\bar{\psi}^{(2)} \to -65^\circ$ as $\bar{e} \to \infty$, and $\bar{\psi}^{(2)} \to 25^\circ$ as $\bar{e} \to -\infty$. In this connection, it should be mentioned that results have also been included in Figs. 10(b) and (d) for the rotation of a "Material Line Element," labeled *MLE*, for comparison purposes. These curves correspond to the rotation of a typical material line element that is initially aligned with the longest axis of the particles (in this case, the axis $\mathbf{e}_3$) in the undeformed configuration, and are determined by the expressions

$$\bar{\psi}^{PS}_{MLE} = -\arctan\left(\frac{\sin(\bar{\theta})\cos(\bar{\theta})(e^{2\bar{e}}-1)}{\sin^2(\bar{\theta})e^{2\bar{e}}+\cos^2(\bar{\theta})}\right), \qquad \bar{\psi}^{AS}_{MLE} = -\arctan\left(\frac{\sin(\bar{\theta})\cos(\bar{\theta})(e^{3\bar{e}}-1)}{\sin^2(\bar{\theta})e^{3\bar{e}}+\cos^2(\bar{\theta})}\right) \tag{18}$$

for pure and axisymmetric shear loadings, respectively. Note that the TSO estimates for the particle rotations are consistent with these results in the limit as the prolate particles become needles ($w \to \infty$).

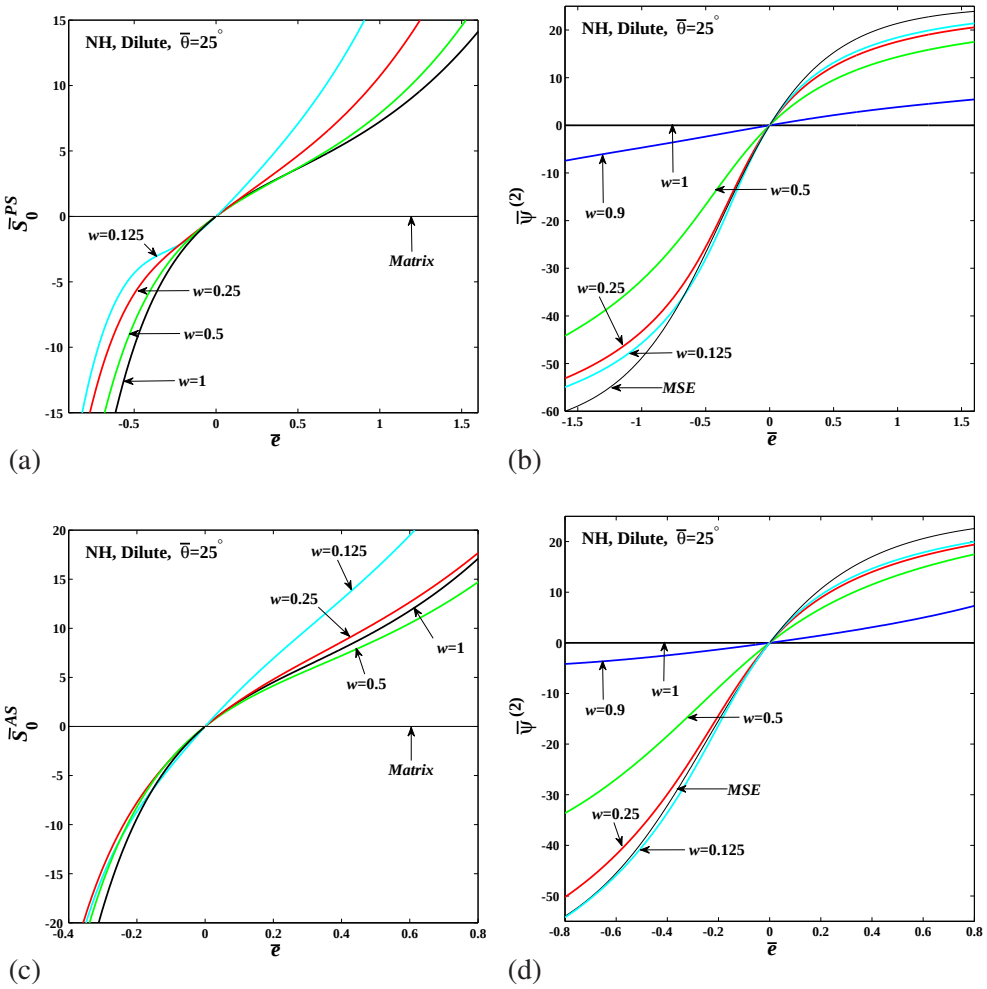

Figure 11. TSO estimates for particle-reinforced neo-Hookean composites with dilute concentrations of *oblate* particles subjected to *non-aligned* loadings at the fixed angle $\bar{\theta} = 25^\circ$. Parts (a) and (b) show results for the effective stress $\bar{S}_0^{PS}$ and the angle of rotation of the particles $\bar{\psi}^{(2)}$, respectively, for *pure shear* ($\bar{\lambda}_1 = \bar{\lambda}, \bar{\lambda}_2 = 1$). Parts (c) and (d) show results for the effective stress $\bar{S}_0^{AS}$ and the rotation $\bar{\psi}^{(2)}$, respectively, for *axisymmetric shear* ($\bar{\lambda}_1 = \bar{\lambda}_2 = \bar{\lambda}$). The results are shown for particle aspect ratios $w = 1, 0.9, 0.5, 0.25, 0.125$, as functions of the macroscopic logarithmic strain $\bar{e} = \ln(\bar{\lambda})$.

Figure 11 presents results for the TSO estimates for the effective response of incompressible, neo-Hookean elastomers reinforced with a dilute concentration of oblate rigid

particles, under non-aligned pure and axisymmetric shear loadings at the fixed loading angle $\bar{\theta} = 25^\circ$. Results are shown for aspect ratios w equal to 1, 0.9, 0.5, 0.25 and 0.125, as functions of the macroscopic logarithmic strain $\bar{e} = \ln(\bar{\lambda})$. Figures 11(a) and (b) show plots for the macroscopic stress $\bar{S}_0^{PS}$ and the rotation of the particles $\bar{\psi}^{(2)}$, respectively, for pure shear loading. Similarly, Figs. 11(c) and (d) show corresponding results for axisymmetric shear. Compared to the previous results for prolate particles, the results of Fig. 11 for oblate particles are roughly the opposite. Thus, the particles in this case undergo the largest rotations (in the opposite direction) for compressive strains ($\bar{e} < 0$), and the rotations are faster for the smallest aspect ratios. In addition, the particles tend to the asymptotic values ($\bar{\psi}^{(2)} \to 25^\circ$ as $\bar{e} \to \infty$, and $\bar{\psi}^{(2)} \to -65^\circ$ as $\bar{e} \to -\infty$), as long as the aspect ratio w is different from unity (when the particles do not rotate). Correspondingly, the plots for the effective stress-strain relations of the composites exhibit *softening* for compressive strains ($\bar{e} < 0$), and the level of softening increases with decreasing values of the aspect ratio w. On the other hand, the (positive) particle rotations for tensile strains ($\bar{e} > 0$) can be seen to lead to a *stiffening* of the macroscopic stress-strain relation, which becomes progressively more significant, the smaller the aspect ratio.

In Figs. 11 (b) and (d), we have also included plots for the rotation of the normal to a "material surface element" (*MSE*) whose normal is initially aligned with the $\mathbf{e}_3$ axis. This rotation can be expressed as

$$\bar{\psi}_{MSE}^{PS} = \arctan\left(\frac{\sin(\bar{\theta})\cos(\bar{\theta})(\mathrm{e}^{2\bar{e}}-1)}{\sin^2(\bar{\theta})+\mathrm{e}^{2\bar{e}}\cos^2(\bar{\theta})}\right), \quad \bar{\psi}_{MSE}^{AS} = \arctan\left(\frac{\sin(\bar{\theta})\cos(\bar{\theta})(\mathrm{e}^{3\bar{e}}-1)}{\sin^2(\bar{\theta})+\cos^2(\bar{\theta})\mathrm{e}^{3\bar{e}}}\right) \tag{19}$$

for pure and axisymmetric shear loading, respectively. In this connection, it is noted that the TSO estimates for the rotation of oblate particles become consistent with these results for *MSEs* in the limit as the aspect ratio $w \to 0$.

Finally, Fig. 12 provides results showing the influence of the particle volume fraction on the TSO estimates for the effective response of the composites subjected to non-aligned pure and axisymmetric shear loadings. The results in this figure are shown for an incompressible, neo-Hookean elastomer reinforced with rigid, prolate particles with a fixed aspect ratio, $w = 2$, and three concentrations, $c = 0.05, 0.15, 0.25$. In addition, the results are shown for two loading angles $\bar{\theta} = 5^\circ$ and 25°, as functions of the macroscopic logarithmic strain $\bar{e} = \ln(\bar{\lambda})$. Similar to the previous figures in this subsection, parts (a) and (b) show pure shear results for the macroscopic stress $\bar{S}_0^{PS}$ and the rotation of the particles $\bar{\psi}^{(2)}$, respectively, while parts (c) and (d) show the corresponding results for axisymmetric shear. The main observation from these figures is that the particle concentration c has a relatively small effect on the particle rotations (in fact, for small strains the particle rotations are completely insensitive to c), while it has a significant effect on the effective stress-strain relations for the composites. Thus, we can see that, as expected, increasing values of c result in stiffer responses both in tension and compression, as well as for both pure and axisymmetric shear. On the other hand, we also observe that the initial loading angle has a significant effect on the particle rotations, but a relatively small influence on the macroscopic stress-strain relation for the composite. In addition, consistent with the results of Fig. 4, it can be seen that the reinforced elastomers become less stable with increasing particle volume fractions, while the response of these composites is more stable for the larger loading angle (25°), where loss of ellipticity is not detected for the levels of strain considered.

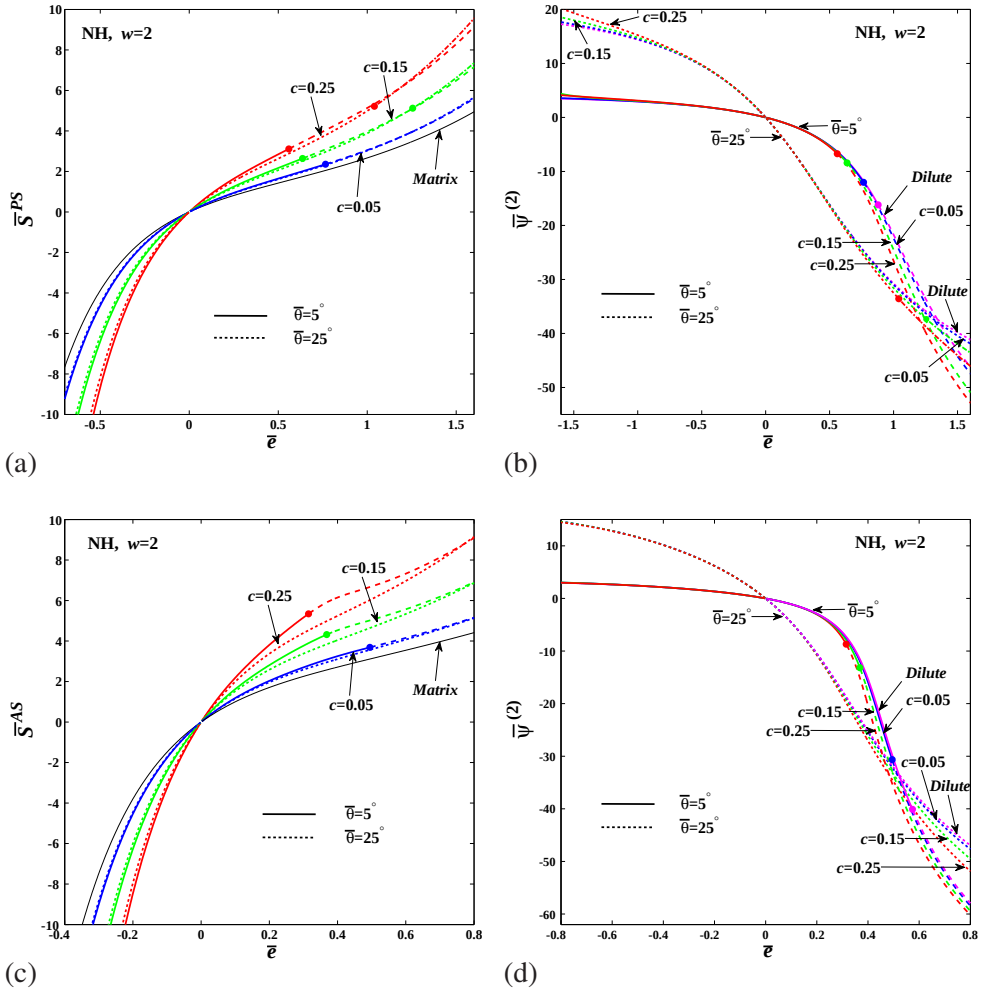

Figure 12. TSO estimates for a particle-reinforced neo-Hookean composite with prolate particles of aspect ratio $w = 2$ subjected to *non-aligned* loadings at the angles $\bar{\theta} = 5°$, and $25°$. Parts (a) and (b) show results for the case of *pure shear* loading ($\bar{\lambda}_1 = \bar{\lambda}$, $\bar{\lambda}_2 = 1$), respectively for the effective stress $\bar{S}_0^{PS}$ and the angle of rotation of the particles $\bar{\psi}^{(2)}$. Parts (c) and (d) show results for the case of *axisymmetric shear* loading ($\bar{\lambda}_1 = \bar{\lambda}_2 = \bar{\lambda}$), respectively for the effective stress $\bar{S}_0^{AS}$ and the rotation $\bar{\psi}^{(2)}$. The results are shown for particle volume fractions $c = 0.05$, 0.15, and 0.25, as functions of the macroscopic logarithmic strain $\bar{e} = \ln(\bar{\lambda})$.

4. Concluding Remarks

In this paper, we made use of the tangent second-order (TSO) constitutive model presented in Part I to generate estimates for the homogenized stress-strain relation, the evolution of microstructure, and the onset of macroscopic instabilities in particle-reinforced elastomeric composites consisting of an incompressible Gent/neo-Hookean matrix and random distributions of aligned spheroidal particles of aspect ratio w. The estimates presented in this paper provide a broad picture of the influence of the macroscopic loading conditions, matrix properties and microgeometry (including particle volume fractions and shapes) on the effective behavior and the possible onset of macroscopic instabilities in the composites. Explicit results are given for composites with both *prolate* and *oblate* spheroidal shapes, subjected to *aligned* and *non-aligned* pure shear and axisymmetric shear loading conditions. These results generalize the recent results of Avazmohammadi and Ponte and Castañeda [3] for elastomers reinforced with random distributions of spherical particles ($w = 1$), as well as earlier results of Lopez-Pamies and Ponte Castañeda [8] for 2-D composites reinforced with elliptical fibers. In addition, the results of this work are consistent with earlier results for laminated elastomers [4, 11] and for continuous-

fiber-reinforced elastomers [1] in the limits as the aspect ratio w tend to zero and ∞, respectively.

Concerning the results for the overall behavior, we begin by emphasizing that the TSO model predictions are in very good agreement with available numerical results [7] for spherical particles ($w = 1$), up to fairly large strains. Similarly, the TSO results were found to be in excellent agreement with FEM results [13] for the transverse shear response of continuous-fiber-reinforced elastomers ($w \to \infty$). In particular, it should be emphasized that the new choice for the response of the neo-Hookean matrix phase, as given by expression (3), leads to estimates for the macroscopic stress-strain relation that do not lock up at finite strains. This is different from the corresponding expressions given in [3], which tend to lock up at a finite strain that becomes smaller with increasing particle volume fraction, even for neo-Hookean matrix behavior. Although a very minor change relative to the expressions originally given in [3] (nothing else changes!), the use of the new expression does give much better agreement with the available numerical results, especially at the larger volume fractions. It should be noted, however, that the corresponding results for reinforced Gent elastomers do exhibit significant stiffening due to the particles, and tend to lock up at strains that are smaller than for the elastomeric matrix material and that become smaller with increasing particle volume fraction.

Compared to the results for spherical particles, it is found that the corresponding results for prolate, or oblate particles generally result in stiffer responses when the reinforced elastomers are loaded in pure shear or axisymmetric shear aligned with the particle axes, and the amount of stiffening increases with increasing (decreasing) aspect ratio for prolate (oblate) particles. However, when the loading axes are not aligned with the particle axes, it is found that the particles may undergo significant rotations tending to align their long axes with the tensile axes of loading; this phenomenon in turn may lead to significant softening, which becomes more pronounced as the particle shape moves away from spherical. In fact, when the tensile loading axis is nearly orthogonal to the long axes of the particles, the particles can suddenly undergo large rotations at a certain critical amount of straining, which is found to be coincident (at least for dilute concentrations) with the vanishing of the shear component of the incremental effective elasticity tensor transverse to the long particle axis of the reinforced elastomer. Thus, the reinforced elastomers with spheroidal particles can undergo shear localization instabilities, which are captured by loss of ellipticity of the associated effective incremental modulus tensors, and correspond physically to the sudden collective rotation—or flopping—of the particles to try to accommodate the imposed deformation. These flopping-type macroscopic instabilities in short-fiber-reinforced elastomers were first predicted theoretically in the context of model 2-D composites by Lopez-Pamies and Ponte Castañeda [8] and verified numerically by Michel et al. [12] for the same type of 2-D composites. Although the physical mechanism for these symmetry-breaking instabilities is essentially the same for the more realistic 3-D composites considered in this work, the behavior is a bit richer for the 3-D composites when subjected to general 3-D loadings since the particles tend to flop in the softest direction (the one associated with the first transverse shear modulus to vanish). Also, consistent with earlier findings for the 2-D composites, the reinforced elastomers become more unstable (i.e., they develop instabilities for smaller strains) as the particle shape moves away from the perfectly symmetric spherical shapes and as the volume fraction of the particles increases.

Finally, it should be emphasized that although the constitutive models developed in this work are approximate, they have significant advantages relative to full field numerical simulations. First, the numerical simulations of these problems are difficult due to the large stretches involved (requiring remeshing and other sophisticated numerical techniques) and are computationally very intensive (in practice, relatively small numbers of particles can be considered and ensemble averages would be required). As a consequence,

to the knowledge of the authors, results are not yet available beyond the already mentioned results for spherical particles and model 2-D composites. Second, in practical applications, it is necessary to solve boundary value problems with non-uniform boundary conditions and complicated geometries. This requires the use of the finite element method, and for this purpose, it is crucial to be able to determine the homogenized response of the composite material accurately and efficiently under general loading conditions. Clearly, this is something that would be difficult to accomplish numerically with current codes and computational power for these highly nonlinear, anisotropic materials, but is something that would be feasible using the analytical constitutive models developed in this work. It should be also noted that the results obtained in this work could be generalized to account for more general microstructures, including random particle orientations, as well as other phases (e.g., voids [9, 10]), by making use of suitable "linear comparison media" in the context of the tangent second-order homogenization technique. In addition, the models developed in this work could be used directly to generate corresponding models for magneto-active elastomers (or dielectric elastomer composites) by means of the partial decoupling approximation [14, 15]. These and other applications will be the subject of future work.

Acknowledgements

This material is based upon work supported by the National Science Foundation under Grant No. CMMI-0969570. Parts of this article were written while PPC was visiting IMDEA Materials Institute in Madrid, Spain.

References

[1] Agoras, M., Lopez-Pamies, O., Ponte Castañeda, P., 2009a. A general hyperelastic model for incompressible fiber-reinforced elastomers. J. Mech. Phys. Solids 57, 268–286.
[2] Agoras, M., Lopez-Pamies, O., Ponte Castañeda, P., 2009b. Onset of macroscopic instabilities in fiber-reinforced elastomers at finite strain. J. Mech. Phys. Solids 57, 1828–1850.
[3] Avazmohammadi, R., Ponte Castañeda, P., 2013. Tangent second-order estimates for the large-strain, macroscopic response of particle-reinforced elastomers. J. Elasticity 112, 139–183.
[4] deBotton, G., 2005. Transversely isotropic sequentially laminated composites in finite elasticity. J. Mech. Phys. Solids 53, 1334–1361.
[5] Eshelby, J., 1957. The determination of the elastic field of an ellipsoidal inclusion and related problems. Proc. R. Soc. Lond. A 241, 376–396.
[6] Geymonat, G., Müller, S., Triantafyllidis, N., 1993. Homogenization of nonlinearly elastic materials, microscopic bifurcation and macroscopic loss of rank-one convexity. Arch. Rat. Mech. Anal. 122, 231–290.
[7] Lopez-Pamies, O., Goudarzi, T., Nakamura, T., 2013a. The nonlinear elastic response of suspensions of rigid inclusions in rubber: I, An exact result for dilute suspensions. J. Mech. Phys. Solids 61, 19–37.
[8] Lopez-Pamies, O., Ponte Castañeda, P., 2006b. On the overall behavior, microstructure evolution, and macroscopic stability in reinforced rubbers at large deformations: II — Application. J. Mech. Phys. Solids 54, 831–863.
[9] Lopez-Pamies, O., Ponte Castañeda, P., 2007a. Homogenization-based constitutive models for porous elastomers and implications for macroscopic instabilities: I—Analysis. J. Mech. Phys. Solids 55, 1677–1701.
[10] Lopez-Pamies, O., Ponte Castañeda, P., 2007b. Homogenization-based constitutive models for porous elastomers and implications for macroscopic instabilities: II—Results. J. Mech. Phys. Solids 55, 1702–1728.
[11] Lopez-Pamies, O., Ponte Castañeda, P., 2009. Microstructure evolution in hyperelastic laminates and implications for overall behavior and macroscopic stability. Mech. Mater. 41, 364–374.
[12] Michel, J., Lopez-Pamies, O., Ponte Castañeda, P., Triantafyllidis, N., 2010. Microscopic and macroscopic instabilities in finitely strained fiber-reinforced elastomers. J. Mech. Phys. Solids 58, 1776–1803.
[13] Moraleda, J., Segurado, J., Llorca, J., 2009. Finite deformation of incompressible fiber-reinforced elastomers: A computational micromechanics approach. J. Mech. Phys. Solids 57, 1596–1613.
[14] Ponte Castañeda, P., Galipeau, E., 2011. Homogenization-based constitutive models for magnetorheological elastomers at finite strain. J. Mech. Phys. Solids 59 (19), 194–215.
[15] Ponte Castañeda, P., Siboni, M. H., 2012. A finite-strain constitutive theory for electro-active polymer composites via homogenization. Int. J. of Nonlinear Mech. 47 (2), 293–306.
[16] Willis, J., 1977. Bounds and self-consistent estimates for the overall moduli of anisotropic composites. J. Mech. Phys. Solids 25, 185–202.